THE JOURNAL OF PHYSICAL CHEMISTRY C
A JOURNAL OF THE AMERICAN CHEMICAL SOCIETY

pubs.acs.org/JPCC Article

Theoretical and Experimental Assessments of Elementary Steps and Bound Intermediates in Catalytic H_2–O_2 Reactions on Dispersed Pt Nanoparticles

Haefa Mansour and Enrique Iglesia*

Cite This: J. Phys. Chem. C 2023, 127, 4553–4569 Read Online

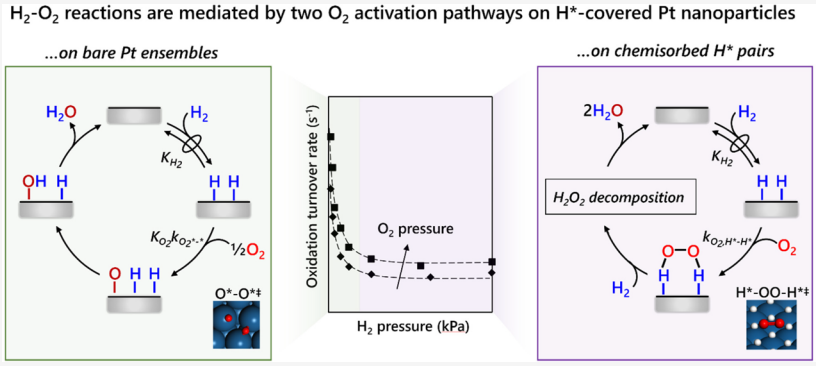

ABSTRACT: Kinetic and isotopic data and H_2 chemisorption uptakes measured under reaction conditions are combined here with theoretical assessments on model catalytic surfaces at relevant hydrogen (H*) coverages to establish the identity and kinetic relevance of elementary steps and bound species in H_2–O_2 reactions on Pt surfaces. Turnover rates are proportional to O_2 pressure and decrease and then reach constant values as H_2 pressures increase, leading to apparent first-order rate parameters (r_{O_2}/P_{O_2}) that reflect reactive collision probabilities of O_2 with surfaces and which depend solely on the H_2 pressure at all temperatures (540–680 K). H_2–D_2 isotopic exchange rates during reactions with O_2 are much faster than water formation rates, consistent with quasi-equilibrated H_2 dissociation steps and with prevalent H* coverages that can be determined independently from H_2 uptakes; such measurements enable the decoupling of non-Langmuirian adsorption parameters from kinetic parameters in rate equations. These data indicate that H_2–O_2 reactions involve two kinetically-relevant O_2 dissociation routes. One channel forms two bound O atoms on bare Pt atom ensembles available within H* adlayers, which react via fast subsequent reactions with H* to form H_2O. A parallel O_2 dissociation route involves reactions with a H*–H* pair to form weakly bound adsorbed hydrogen peroxide (*HOOH*), a highly reactive species that subsequently cleaves its O–O bond in steps that are not kinetically-relevant. The free-energy barriers are dominated by losses in translational entropy incurred upon the formation of the transition states from their gaseous O_2 precursors. Kinetic isotope effects are near unity for both routes because H* is not involved in direct O_2 dissociation steps, and the *HOOH* formation transition state occurs very early along the reaction coordinate (with nearly intact O–O and Pt–H bonds from reactant states), as confirmed by DFT-derived energies and isotope effects.

1. INTRODUCTION

The oxidation of H_2 by O_2 to form H_2O on Pt surfaces, first reported by Davy[1] and later by Döbereiner and Faraday,[2,3] is arguably the earliest documented example of surface catalysis and the subject of many later studies.[4–12] These reactions can be used to scavenge H_2 formed during the dehydrogenation of organic molecules, thus increasing attainable yields through equilibrium shifting,[13–15] and in hydrogen fuel cells;[16] they are also likely to mediate the partial oxidation of CH_4 to synthesis gas.[17,18] Such diverse applications, taken together with the seemingly simple nature of the molecules involved, have served to fuel persistent inquiries into the mechanistic details of these reactions. Equilibrium limits in alkane dehydrogenation catalysis can be circumvented by scavenging H_2 with O_2 on Pt-based catalysts.[13–15] These equilibrium-shifting strategies require mechanistic assessments of H_2–O_2 reactions at temperatures and H_2/O_2 ratios higher than the near-ambient temperatures and stoichiometric reactant mixtures typically

Received: December 16, 2022
Revised: February 7, 2023
Published: February 27, 2023

https://doi.org/10.1021/acs.jpcc.2c08826
J. Phys. Chem. C 2023, 127, 4553–4569

addressed (273−463 K).[5,8,10,11] The high turnover rates under these conditions, taken together with the highly exothermic nature of these reactions (ΔH° = −572 kJ/mol of O_2),[19] can lead to severe gradients in concentrations and temperature within aggregates and reactors. Such corruptions of measured rates by transport effects tend to obscure the chemical origins of kinetic data; they must be avoided through extreme levels of dilution on the bed and catalyst aggregate scales or accounted for through reaction-transport models that require physical properties (e.g., diffusivities, conductivities, and void fractions) that are seldom reported or measured. Mechanistic inferences from accurate rate data must then be benchmarked against theoretical treatments, such as density functional theory (DFT), using realistic models of active surfaces at the coverages of bound reactants and reactive intermediates relevant to the practice of these reactions.

H_2−O_2 reactions on Pt surfaces involve simple molecules and by inference simple rearrangements, thus rendering them also attractive as probes of fundamental concepts in surface catalysis. Their apparent stoichiometric simplicity has not led, however, to unequivocal mechanistic conclusions; this reflects, in part, coverage effects from bound intermediates that cannot be accurately described using Langmuirian formalisms at the high prevalent coverages of bound species and also because of the aforementioned transport artifacts. These previous Langmuirian treatments have implicated elementary steps of the dissociation of O_2 and H_2 and the recombination of bound H (H*) and O (O*) atoms to form OH* and ultimately H_2O*.[20−23] Such conclusions were reached based on measured kinetic trends at pressures (<0.1 kPa) much lower than relevant to catalytic practice and at low H* and O* coverages; such studies also do not assign specific kinetic relevance to the proposed elementary steps involved in H_2−O_2 reactions.[20−23] Another study concluded that O_2 dissociation to O* is the sole kinetically-relevant step based on DFT-derived energies calculated for essentially bare Pt(111) surfaces (15 kPa H_2, 7 kPa O_2, 773 K);[7] such routes do not fully capture kinetic trends measured at higher pressures, such as rates that become insensitive to H_2 pressure on H*-saturated Pt surfaces,[5] which reveal the involvement of alternate pathways relevant at higher H* or O* coverages.

Here, H_2−O_2 reaction rates were measured under conditions of strict kinetic control and combined with DFT treatments to examine the identity and kinetic relevance of elementary steps and bound species on dispersed Pt nanoparticles at H_2/O_2 ratios above unity and high temperatures (500−700 K); these conditions are particularly suitable for oxidative H_2 scavenging during alkane dehydrogenation reactions. Kinetic and isotopic methods show that rates reflect contributions from two parallel kinetically-relevant steps involving the O_2 reactions with (i) vicinal unoccupied surface Pt atoms (*) and (ii) vicinal bound H atoms (H*) formed via quasi-equilibrated H_2 dissociation. Alkane oxidation reactions, in contrast, involve only the former O_2 activation route.[24,25] The latter route may account for the remarkable selectivity for H_2−O_2 reactions (over hydrocarbon−O_2 reactions) in dehydrogenation equilibrium-shifting strategies[14,15] because O_2 is able to react directly with bound H*, but C−H activation steps require access to bare surface atoms.

DFT-derived binding energies of intermediates and transition states are consistent with those of such O_2 activation pathways. They show that O_2 binds molecularly on bare Pt surfaces to form O_2* species that dissociate to form O* in essentially barrierless steps; the presence of H*, however, decreases the mean size of unoccupied Pt ensembles within H* adlayers, causing O_2 dissociation barriers to increase as H_2 pressures and H* coverages increase. These H* coverage effects are not captured by Langmuirian kinetic models, yet such formalisms lead to rate equations that can faithfully describe H_2−O_2 rates because of the "forgiving" nature of the functional form of Langmuirian rate equations and the limited range of reactant pressures in most kinetic studies.[26] Reactions of O_2 in gaseous or weakly-bound forms with H*−H* pairs to form bound hydroperoxide species (*HOOH*) become the predominant route at high H* coverages. The resulting *HOOH* species ultimately decompose to H_2O via facile thermal- or surface-catalyzed pathways. Measured activation barriers for direct O_2 dissociation on bare Pt ensembles (31 ± 2 kJ mol^{-1}) and for O_2 reactions with H*−H* pairs (31 ± 4 kJ mol^{-1}) are the same; the relative contributions to rates from each pathway reflect the different entropies of formation of their respective transition states and the prevalent H* coverages. H-assisted O_2 activation routes become more prevalent as the temperature decreases because of higher H* coverages at lower temperatures and the dearth of vacant sites for direct O_2 activation steps. These findings underscore the need for experimental and theoretical assessments that involve realistic surfaces at the adsorbate coverages relevant to steady-state catalysis in practice.

2. METHODS

2.1. Catalyst Synthesis and Characterization. SiO_2 (Davisil 646, 300 m^2 g^{-1}) was treated in flowing dry air (Praxair, 99.99%, 10 cm^3 g^{-1} s^{-1}) by heating to 898 at 0.03 K s^{-1} and holding for 5 h. Pt/SiO_2 catalysts were prepared by using strong electrostatic adsorption methods with Pt-$(NH_3)_4(NO_3)_2$ complexes (Sigma-Aldrich, 99.9%) grafted onto treated SiO_2 from a 0.4 M NH_4OH solution (10 cm^3 g^{-1} SiO_2) by stirring the suspension for 2 h.[27] Solids were recovered by vacuum filtration, rinsed with deionized water (≥17.6 mΩ cm; 200 cm^3 H_2O per g of solid), and treated in ambient air overnight at 368 K. The Pt content and treatment protocols were varied to obtain samples with different mean Pt nanoparticle diameters (1.7−6.2 nm, measured as described below). Pt/SiO_2 catalysts with 1.5 wt % Pt content were treated at two different temperatures (673 or 873 K) by heating at 0.05 K s^{-1} in flowing dry air (Praxair, 99.99%, 10 cm^3 g^{-1} s^{-1}) and holding for 6 h to create samples with mean nanoparticle diameters of 1.7 and 6.2 nm, respectively. Pt/SiO_2 catalysts with 0.2 wt % Pt content were treated at 873 K by heating at 0.05 K s^{-1} in flowing dry air (Praxair, 99.99%, 10 cm^3 g^{-1} s^{-1}) and holding for 6 h to prepare a sample with a mean nanoparticle diameter of 2.3 nm. Samples were cooled to ambient temperature and then heated to 773 at 0.05 K s^{-1} in flowing 50% H_2/He (Praxair, 99.999%, 10 cm^3 g^{-1} s^{-1}) and held for 6 h to form metallic Pt nanoparticles; they were then brought to ambient temperature and treated in flowing 2% O_2/He (Praxair, 99.99%, 5 cm^3 g^{-1} s^{-1}) to passivate the nanoparticle surfaces before exposure to ambient air.

The Pt content in each sample was measured by inductively coupled plasma optical emission spectroscopy (ICP-OES; Galbraith Laboratories). Pt dispersions and mean nanoparticle diameters were determined from measured volumetric uptakes of chemisorbed hydrogen at 373 K by assuming a 1:1 H/Pt_s (Pt_s denotes surface Pt atoms) stoichiometry. Samples (previously treated as described above) were exposed to

https://doi.org/10.1021/acs.jpcc.2c08826
J. Phys. Chem. C 2023, 127, 4553−4569

flowing H_2 at 623 K (Praxair, 99.999%, 1 cm^3 g^{-1} s^{-1}) for 1 h and evacuated (<10^{-2} mbar) for 1 h using a rotary vane pump (Leybold, Trivac D2.5E) and a turbomolecular pump (Pfeiffer Vacuum, TMU 071 P) before uptake measurements. H_2 uptakes were measured by sequential H_2 doses to achieve final pressures between 0.02 and 80 kPa H_2. Surface-averaged mean particle diameters were determined from Pt dispersion values using the following equations

$$d_{chem} = \frac{6v_m/a_m}{D}\theta_{sat} \quad (1)$$

$$\theta_{sat} = 1 + \alpha d_{chem}^{-1} + \beta d_{chem}^{-2} \quad (2)$$

where v_m is the specific volume of bulk Pt metal per Pt atom (15.1×10^{-3} nm^3), a_m is the surface area occupied by an surface atom in bulk Pt crystals (8.1×10^{-2} nm^2), D is the metal dispersion, and α and β are semiempirical parameters determined from DFT assessments of saturation coverages as a function of particle size (0.0364 and 0.735 respectively).[28,29]

2.2. H_2−O_2 Reaction Rate Measurements. H_2 oxidation turnover rates were measured in a packed-bed tubular reactor (quartz, 4 mm I.D.) with plug-flow hydrodynamics at 548−673 K. The bed temperature was maintained using a resistively-heated three-zone furnace and measured with a K-type thermocouple in contact with the outer reactor wall. Quartz rods were placed within the inlet and outlet regions of the catalyst to minimize heated volumes (to 1.5 cm^3 of total reactor volume) and contributions from homogeneous H_2−O_2 reactions.

Pt/SiO_2 catalysts were diluted with SiO_2 (Davisil 646, 300 m^2 g^{-1}) previously treated in flowing dry air (Praxair, 99.99%, 10.0 cm^3 g^{-1} s^{-1}) by heating to 898 at 0.03 K s^{-1} and holding for 5 h. The effects of intraparticle dilution (SiO_2-to-catalyst mass ratios, λ = 400−800) on measured rates were used to assess (and avoid) corruption of the measured rates by temperature or concentration gradients. Diluted powders were pelleted to retain 180−250 μm aggregates and then mixed with quartz powder (Sigma-Aldrich, no. 204358) at quartz-to-catalyst mass ratios (χ) ranging from 1000 to 30 000 to assess and avoid any temperature gradients at the bed scale. Measured rates that did not depend on the extent of dilution at the aggregate and bed scales confirmed the absence of hydrodynamic and transport artifacts.

Inlet molar rates were metered using electronic mass flow controllers (Parker, model 201). Pretreated and passivated samples were treated again within the reactor in flowing 25% H_2/He (Praxair, 99.999%, 7×10^9 cm^3 g-atom Pt^{-1} s^{-1}) by heating to 723 at 0.083 K s^{-1} and holding for 1 h. The composition of the inlet stream was set by mixing H_2 (Praxair, 99.999%), 20% O_2/He (Praxair, 99.9%), and He (Praxair, 99.999%). H_2 pressures were varied between 1 and 80 kPa, and O_2 pressures were varied between 0.25 and 2 kPa; combined H_2 and diluent pressures were kept above the upper flammability limit (the highest possible concentration of H_2 in a H_2−O_2 mixture at which a flammable mixture is formed) for safe operations.[30] All rates were measured at low conversions (<10% H_2 or O_2 conversion), and differential reactor treatments were used in all kinetic analyses; such differential reactor formalisms require the absence of significant product inhibition (demonstrated in section S1.2, SI). H_2O effluent concentrations were measured by gas chromatography (Agilent GC, 6890) using a packed column (Porapak Q, 2.74 m length, 2 mm I.D.) and thermal conductivity detection. O_2 consumption turnover rates (r_{O_2}) are reported as the molar rate of conversion of O_2 to H_2O per surface Pt atom in each sample (from H_2 uptakes measured at 373 K; section 2.1).

D_2 (Praxair, 99.8% isotopic enrichment) was also added to the H_2−O_2 reactant mixture to probe the reversibility of hydrogen dissociation steps (from HD formation rates using online mass spectrometry; MKS Instruments, Mini-Lab). The approach to equilibrium for H−D isotopic exchange (η_{exch}) was determined by comparing the HD mole fraction in the effluent stream (denoted as μ) to that in an isotopically equilibrated mixture (μ_{equil}), which would be described by a binomial isotopologue distribution

$$\eta_{exch} = \frac{\mu}{\mu_{equil}} \quad (3)$$

$$\mu_{equil} = 2\lambda(1 - \lambda) \quad (4)$$

where λ is the H content in the H_2−D_2 inlet stream.

2.3. Density Functional Theory (DFT) Methods. Spin-polarized plane-wave DFT calculations were carried out using the Vienna *ab initio* simulation package (VASP).[31−33] Plane waves were constructed using projector-augmented wave (PAW) potentials with an energy cutoff of 396 eV[34,35] and an 8 × 8 × 1 Monkhorst−Pack k-point sampling.[36] Electronic energies were determined using the generalized gradient approximation (GGA) with Perdew−Wang 91 (PW91) and revised Perdew−Burke−Ernzerhof (RPBE) exchange-correlation functionals;[37] both functionals were used in order to compare DFT-derived energies in this study with those calculated in previous DFT studies of O_2 activation on Pt_{201} nanoparticles (PW91)[24] and H_2 activation on Pt(111) surfaces (RPBE and PW91).[26] Wave functions were converged to electronic energies of <10^{-6} eV and geometries until forces on all atoms were <0.05 eV $Å^{-1}$ between iterations.

Pt(111) surfaces were modeled as a 4 × 4 periodic lattice with four layers in the z direction and 1.5 nm of vacuum between the four-layer slabs. The (111) plane was chosen because it is among the most prevalent facets for Pt nanoparticles larger than 2 nm.[38] The bottom two layers were held at their bulk positions (0.3924 nm lattice constant[39]), and the top two layers were relaxed to their minimum-energy structures in all iterations. H atoms can bind in atop, 3-fold fcc, and 3-fold hcp positions on Pt(111) surfaces at relevant reaction temperatures. The 3-fold fcc and atop binding modes are the most stable binding modes;[26] they were used as the initial structures for calculating the energies of transition states and intermediates at each H* coverage. Gaseous molecules were placed in a vacuum within a 20 × 20 × 20 Å unit cell in energy calculations.

Transition state (TS) structures were determined for each elementary step by using nudged elastic band (NEB)[40,41] and dimer[42] methods. NEB calculations were carried out using eight images with energy and force convergence criteria of 10^{-4} eV and 0.1 eV $Å^{-1}$, respectively. The Henkelman dimer algorithm[43] was used to refine such structures with the same energy and force convergence criteria as those in all other optimizations.

Vibrational frequencies of reactant and TS structures were calculated from the Hessian matrix of second derivatives of energies with respect to atomic position, fixing the positions of all metal atoms in order to decrease computational require-

https://doi.org/10.1021/acs.jpcc.2c08826
J. Phys. Chem. C 2023, 127, 4553−4569

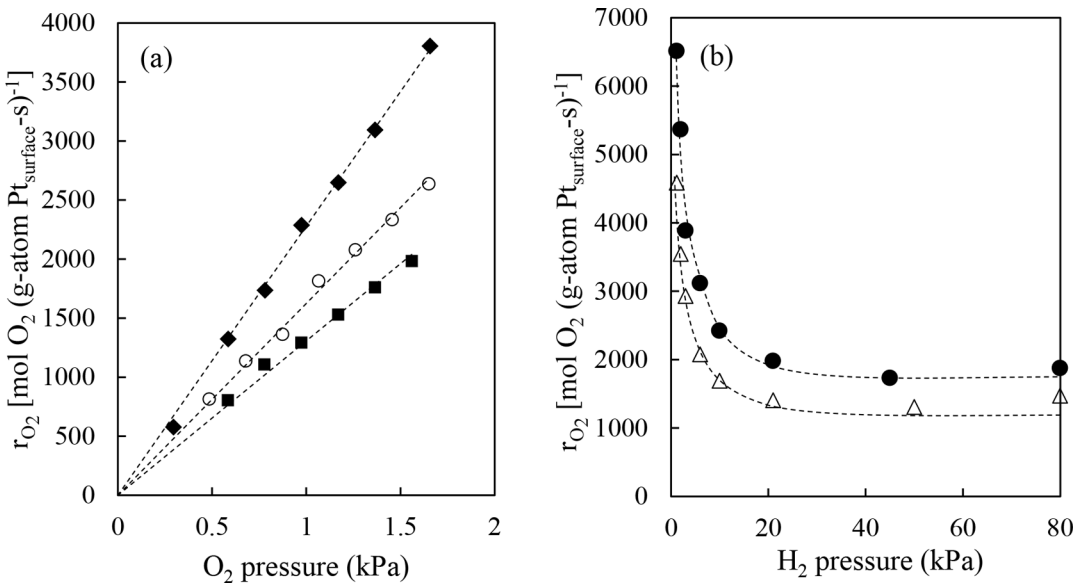

Figure 1. (a) O_2 turnover rates during H_2−O_2 reactions at 5 (♦), 10 (○), and 20 kPa (■) H_2 at 603 K. (b) O_2 turnover rates during H_2−O_2 reactions at 1 kPa (Δ) and 1.5 kPa (●) O_2 at 603 K (0.2 wt % Pt/SiO_2, 2.3 nm mean cluster size). Dashed curves are shown to guide the eye and indicate trends.

ments. Low vibrational frequencies (<60 cm^{-1}), which tend to contribute significantly to entropies and are not accurately determined by harmonic oscillator DFT methods, were replaced with a frequency of 60 cm^{-1}, as was done in previous studies of NO−H_2 reactions on Rh(111) surfaces[44] and propanol dehydration on HZSM-5.[45,46] These frequencies were used to obtain zero-point vibrational energies (ZPVE) and vibrational enthalpies (H_{vib}), entropies (S_{vib}), and free energies (G_{vib})

$$\mathrm{ZPVE} = \sum_i \left(\frac{1}{2}h\nu_i\right) \tag{5}$$

$$H_{vib} = \sum_i \left(\frac{h\nu_i e^{-h\nu_i/kT}}{1 - e^{-h\nu_i/kT}}\right) \tag{6}$$

$$S_{vib} = \sum_i \left(\frac{1}{T}\frac{h\nu_i e^{-h\nu_i/kT}}{1 - e^{-h\nu_i/kT}} - k \ln \frac{1}{1 - e^{-h\nu_i/kT}}\right) \tag{7}$$

$$G_{vib} = \sum_i \left(-kT \ln \frac{1}{1 - e^{-h\nu_i/kT}}\right) \tag{8}$$

where k and h are the Boltzmann and Planck constants, T is the absolute temperature, and ν_i represents the vibrational frequencies. Gibbs free energies (G) and enthalpies (H) of reactants and transition states were calculated from DFT-derived energies and vibrational frequencies and, for gaseous molecules, from statistical mechanics (details in Supporting Information, SI; S2.1):

$$H = E_0 + \mathrm{ZPVE} + H_{vib} + H_{trans} + H_{rot} \tag{9}$$

$$G = E_0 + \mathrm{ZPVE} + G_{vib} + G_{trans} + G_{rot} \tag{10}$$

Kinetic isotope effects (KIE) are defined as the ratio of k_H to k_D, where k_H and k_D are the respective rate constants involved in the reactions of H_2 and D_2 with O_2, respectively. Such values were calculated from the Gibbs free energy of formation of the TS ($\Delta G_H^{\ddagger}$) relative to the Gibbs free energy of formation of the TS when H atoms are replaced by D atoms ($\Delta G_D^{\ddagger}$):

$$\mathrm{KIE} = e^{\left(-\frac{\Delta G_H^{\ddagger} - \Delta G_D^{\ddagger}}{kT}\right)} \tag{11}$$

3. RESULTS AND DISCUSSION

3.1. Kinetic Trends in H_2−O_2 Reaction Rates with Reactant and Product Pressures. H_2−O_2 turnover rates (r_{O_2}, molar O_2 conversion rates per g-atom $Pt_{surface}$) were insensitive to the extent of intraparticle or bed dilution (λ = 400−800; χ = 1000−30 000, respectively, defined in section 2.2) under all conditions used in this study (Supporting Information, S1.1); these levels of dilution are therefore sufficient (and required) to ensure the strict chemical origins of all reported rate data. Turnover rates were also unaffected by changes in the heated empty volume in reactor cells (as described in section 2.2), thus confirming the absence of contributions from the homogeneous H_2−O_2 reactions.

H_2−O_2 turnover rates increased linearly with increasing O_2 pressure (0.3−2 kPa O_2, Figure 1a) at all H_2 pressures; they decreased and ultimately became constant as H_2 pressures increased (1−80 kPa H_2, Figure 1b) for each O_2 pressure. These kinetic trends were similar on samples with a broad range of mean Pt nanoparticle diameters (1.7−6.2 nm; section 3.5). These rate data exhibit two distinct kinetic regimes, heuristically captured at this stage as the combined contributions from two terms in a rate equation:

$$r_{O_2} = r_{O_2,1} + r_{O_2,2} = \alpha\frac{[O_2]}{[H_2]} + \beta[O_2] \tag{12}$$

A mechanism-based rate equation with this functional form that is able to describe measured rates over a broader temperature range (548−673 K) and reactant pressures (1−80 kPa H_2, 0.1−2 kPa O_2) is considered in the next section (section 3.2), but first, the discussion addresses mechanistic insights that can be gained from the functional form of eq 12, for pedagogical and practical purposes in restricting the diverse

https://doi.org/10.1021/acs.jpcc.2c08826
J. Phys. Chem. C 2023, 127, 4553−4569

mechanistic choices to those able to capture these kinetic trends.

The common proportional dependence on the O_2 pressure shown by both terms in eq 12 indicates that both routes are mediated by a TS that contains two O atoms. The inverse H_2 pressure dependence evident in the first term in eq 12 indicates that bound H atoms (H*) are present at kinetically detectable coverages and that H* is the most abundant surface intermediate (MASI) during steady-state catalysis. Rates were not affected by changes in bed residence time that influenced the mean H_2O pressures prevalent during catalysis (0.02 to 0.15 kPa H_2O; Supporting Information, S1.2), consistent with the absence of bound H_2O-derived species at significant coverages or with the involvement of H_2O-mediated proton-coupled electron transfer. Previous studies below 373 K and at higher H_2O pressures (>2 kPa) reported a significant inhibition of H_2 oxidation rates by H_2O, indicating the prevalence of H_2O-derived species at high coverages under such conditions.[47,48] H_2O molecules can act as a cocatalyst by assisting proton-coupled electron-transfer steps in several metal-catalyzed reactions (e.g., CO activation on Ru nanoparticles,[49] CO_2 hydrogenation on Cu(111) surfaces,[50] CO + OH disproportionation on PtRu alloys,[51] and H_2O_2 formation on PtAu nanoparticles in H_2O solvents[52]). The role of H_2O as both a cocatalyst and MASI during CO hydrogenation rates on Co catalysts has led to reports of turnover rates that both increase[53,54] and decrease[53,55] as H_2O pressures increase, depending on the relative contributions of both processes. H_2O-assisted pathways also account for H_2O_2 and H_2O formation on Pt and PtAu nanoparticles in H_2O solvents at low temperatures (286 K), leading to rates that are proportional to H_2O pressure when H_2 dissociation is quasi-equilibrated.[52] At the higher temperatures and lower H_2O pressures addressed in this study, there are no detectable contributions from H_2O-mediated pathways or from surface coverages of H_2O-derived species.

These kinetic data indicate that H_2−O_2 reactions (i) involve two routes (eq 12), each with TS structures containing two O atoms, and (ii) occur on surfaces without detectable coverages of O_2-derived bound species, with H_2-derived species (H* or H_2*) as MASI and * and OH_x* as minority species. H_2* forms as weakly bound precursors that dissociate to H* on Pt surfaces via fast and mildly exothermic steps ($\Delta H_{\cdot}$ = −83 to −75 kJ mol^{-1} at 0.5−1 ML H* coverage on Pt(111) surfaces) that are essentially barrierless ($\Delta H^{\ddagger}$ = 6 to 12 kJ mol^{-1} at 0.5−1 ML H* coverage),[56] consistent with surfaces equilibrated with H_2-derived species and leading to high equilibrium H* coverages.

H_2 dissociation steps are considered to be at equilibrium during H_2−O_2 reactions on metals other than Au (on which they become irreversible and limit rates).[57,58] Quasi-equilibrium requires that H* species recombine to form H_2 at higher rates than for their forward reactions with O_2-derived species to form H_2O. As a result, quasi-equilibration can be probed by comparing rates of isotopic exchange in H_2−D_2−O_2 mixtures (inferred from the formation of HD) and the formation of water. The approach to equilibrium for isotopic exchange (η_{exch}, defined in section 2.2) was less than 0.1 under all conditions in our experiments, indicating that measured isotopic exchange rates approximately represent the forward rate of isotopic exchange. Measured HD formation rates (r_{HD}) represent a fraction of the total recombinative desorption rates because they do not include H−H and D−D recombinations to make H_2 and D_2, respectively. Total recombinative desorption rates (r_{des}) are inferred from the ratio of measured HD formation rates to the fraction of total recombinations (H−H, D−D, and H−D) that is expected to give HD. Assuming that kinetic and thermodynamic isotope effects for H_2 desorption are near unity, the total recombinative desorption rate can thus be described by

$$r_{des} = \frac{r_{HD}}{2\lambda(1-\lambda)} \tag{13}$$

where λ is the H atomic fraction in the inlet stream, a value of 0.5 for the equimolar H_2/D_2 mixtures used here, leading to recombinative desorption rates about 2 times those of HD formation rates.

Figure 2 shows the ratios of the turnover rates for recombinative desorption and H_2 oxidation at different H_2 and D_2 pressures (2−45 kPa H_2 and D_2, equimolar H_2/D_2 mixture, 603 K). Recombination rates were 5−70 times larger than H_2 oxidation rates. These rate ratios increase with increasing total pressure of hydrogen isotopologues because recombinative desorption barriers decrease as H* + D* coverages increase,[26] and H_2 oxidation turnover rates decrease with increasing H_2 pressure (Figure 1b). These data show that H_2 dissociation−recombination steps are quasi-equilibrated during H_2−O_2 reactions, as is often the case during other hydrogenation reactions such as CO−H_2,[59−61] CO_2−H_2,[59] and thiophene−H_2[62] on Pt,[62] Ru,[59,61,62] Re,[62] Co,[60] and Fe[60] metal surfaces under practical reaction conditions (H_2 to coreactant molar ratios much greater than unity).

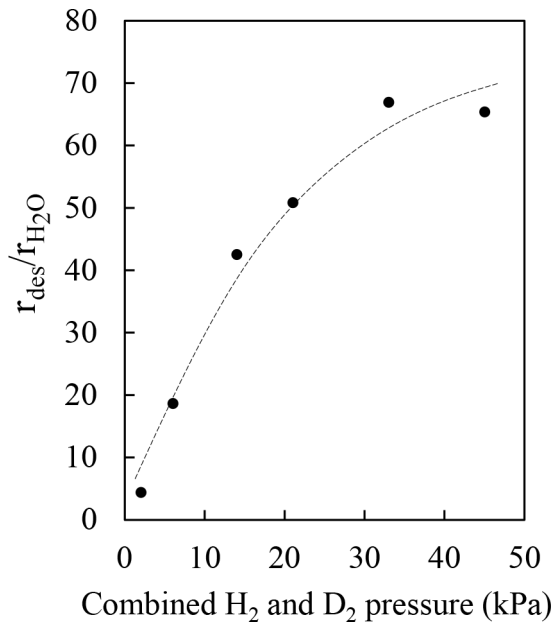

Figure 2. Ratios of total recombinative desorption rates (r_{des}) to H_2O formation rates (r_{H_2O}) at different total (combined) H_2 and D_2 pressures at 603 K, 2−45 kPa H_2 + D_2, (equimolar H_2/D_2 inlet streams), 1.5 kPa O_2 (0.2 wt % Pt/SiO_2, 2.3 nm Pt). The dashed curve is shown to guide the eye and indicate trends.

DFT-derived enthalpies of O_2 dissociation steps (ΔH_{O_2} = −190 kJ/mol of O_2) on bare Pt(111) surfaces are much more negative than for H_2 dissociation (ΔH_{H_2} = −60 kJ/mol of H_2), as shown later (section 3.3) and in previous studies.[26,63] These different O_2 and H_2 dissociation enthalpies would lead to near-

https://doi.org/10.1021/acs.jpcc.2c08826
J. Phys. Chem. C 2023, 127, 4553−4569

saturation O* coverages and to H* present as minority species if these steps were quasi-equilibrated; yet the functional form of H_2-O_2 reaction rate equations (eq 12) precludes kinetically-detectable O* coverages. Thus, oxygen chemical potentials at Pt surfaces during steady-state H_2-O_2 reactions must be significantly lower than those in the contacting fluid phase, a situation that reflects, in turn, the rapid scavenging of O* by H*. The $Pt-Pt_3O_4-PtO_2$ phase diagram[64] indicates that α-PtO_2 forms as the stable form of bulk Pt domains under the conditions of these experiments (0.3−2 kPa O_2, 548−673 K); these thermodynamic data, applicable to bulk Pt systems, become even more favorable for oxidation in the case of nanoparticles because of the lower coordination number of their exposed surface atoms and their concomitantly stronger bonds with O*.[65,66] Thus, equilibrium of O_2 dissociation steps would cause Pt to be present as α-PtO_2 during catalysis.

The quasi-equilibrated nature of H_2 dissociation steps and the low prevalent coverages of O_2-derived species allow the H* coverages during catalysis to be determined from independent measurements of equilibrium H_2 uptakes (in the absence of O_2) at each temperature. These H_2 uptakes show that fractional H* coverages (θ_{H*}; the ratio of H* to the number of surface-metal atoms estimated from nanoparticle diameters from TEM) range from about 0.7 to slightly above unity, as a result of multiple H* at low-coordination Pt surface atoms prevalent on small nanoparticles[29] at the conditions used here for H_2-O_2 reactions (1−80 kPa H_2, 548−673 K).[26] These uptake data can be used to obtain coverages of H* and unoccupied Pt atoms (*) under reaction conditions, which can then be used in evaluating mechanism-based rate equations for H_2-O_2 reactions. The prevalence of H* and * (over O_2-derived bound species) during H_2-O_2 reactions leads to a modified form of eq 12

$$r_{O_2} = r_{O_2,1} + r_{O_2,2} = \frac{\alpha'[O_2]}{(1+\sqrt{K_{H_2}[H_2]})^2} + \frac{\beta'[O_2][H_2]}{(1+\sqrt{K_{H_2}[H_2]})^2} \quad (14)$$

where K_{H_2} is the equilibrium H_2 dissociation constant to form H*.[26] At higher H_2 pressures (and near-saturation coverages), the $(K_{H_2}[H_2])^{0.5}$ denominator term becomes much larger than unity; eq 14 then becomes

$$r_{O_2} = r_{O_2,1} + r_{O_2,2} = \frac{\alpha'[O_2]}{K_{H_2}[H_2]} + \frac{\beta'[O_2]}{K_{H_2}} \quad (15)$$

The functional forms of eqs 12 and 15 are identical, with α and β (in eq 12) now redefined as $\alpha' K_{H_2}^{-1}$ and $\beta' K_{H_2}^{-1}$ (in eq 15).

At high H* coverages, K_{H_2} becomes sensitive to H* coverage because the free energies of species bound at densely covered surfaces are affected by through-space and through-surface repulsion as well as by the loss of entropy caused by hindered H* mobility. Similar trends may also reflect, in part, the intrinsic nonuniformity imposed by Pt atoms of different coordination at nanoparticle surfaces. These coverage-dependent K_{H_2} values render Langmuirian kinetic treatments approximate at best in describing the dynamics of surface catalysis, given that kinetic and thermodynamic parameters for elementary steps vary with coverage.[26] H* coverages can be measured independently from adsorption uptakes[26] in this instance. As a result, there are only two parameters that must be derived from rate data by using a modified form of eq 14

$$r_{O_2} = \alpha[O_2]\theta_*^2 + \beta[O_2]\theta_{H*}^2 \quad (16)$$

where θ_H and θ_* are the fractional coverages of H* and * derived from equilibrium H_2 uptakes. In this manner, the analysis avoids the inherent covariance among kinetic and thermodynamic parameters in the numerator and denominator of eq 14 in regression analyses while also minimizing uncertainties in α and β estimates. H_2-O_2 reaction rates are described faithfully by the functional form of eq 16 at all temperatures (548−673 K), as is evident from the agreement between measured and predicted rates (Figure 3). In spite of

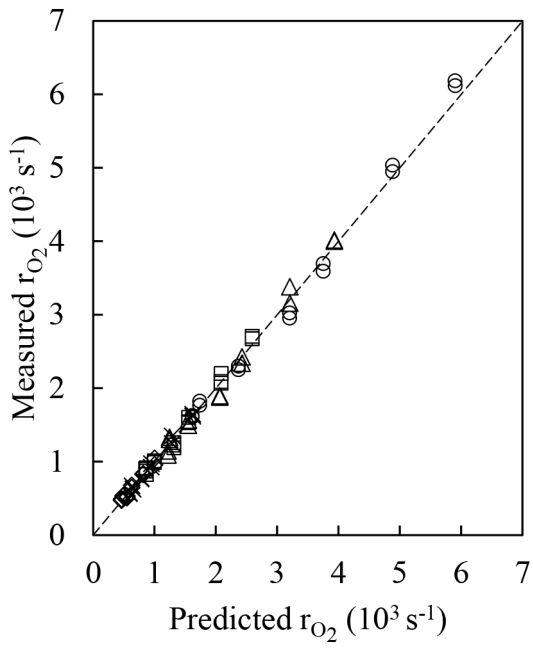

Figure 3. Parity plot for H_2-O_2 reaction rates at 548 K (◇), 573 K (×), 603 K (□), 633 K (Δ), and 673 K (○) [1−50 kPa H_2, 1.5 kPa O_2, balance He; 0.2 wt % Pt/SiO_2, 2.3 nm mean cluster size]. Predicted rates are regressed to the functional form of eq 16.

the apparent accuracy of such a Langmuirian description, it seems likely that α and β will also vary with coverage, in a manner that is not captured by regressed values of rate parameters that seem independent of H_2 pressure (and of its consequences for H* coverage). These are important conceptual matters that are considered in more detail using density functional theory in section 3.3.

3.2. Identity and Kinetic Relevance of Elementary Steps and Bound Species in H_2-O_2 Reactions on Pt Surfaces. The chemical meanings of α and β (eq 16) are examined next through the enumeration and analysis of plausible elementary steps and their kinetic relevance. The evident shift in the kinetic trends with H_2 pressure, from negative to zero-order but with asymptotic rates that do not approach zero values (Figure 1a), requires the involvement of two parallel routes, as reflected in the two terms in eq 16; this requirement is confirmed by DFT methods in sections 3.3 and 3.4.

The TS that mediates the reaction channel that accounts for the first term in eq 16 contains two O atoms and two surface Pt atoms, as evident from rates proportional to O_2 and

https://doi.org/10.1021/acs.jpcc.2c08826
J. Phys. Chem. C 2023, 127, 4553−4569

Scheme 1. Elementary Steps and Bound Species Involved in (a) the Direct O_2 Activation Pathway and (b) the H-Assisted O_2 Activation Pathway to Form H_2O on Pt Surfaces

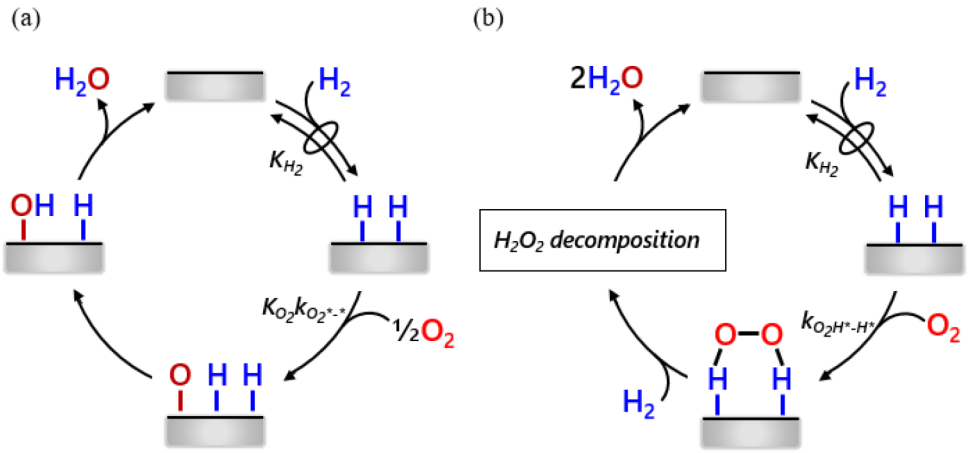

inversely to H_2 pressure on a surface containing significant coverages of H* species in quasi-equilibrium with H_2(g). This step must involve reactions of O_2(g) (or O_2-derived species) at a *−* pair without the additional involvement of any H_2-derived species. These requirements are met by O_2 dissociation at a *−* pair, either in an irreducible elementary event or via sequential formation of weakly-bound O_2* in a quasi-equilibrated step and later reactions with a vicinal * to form O*−O* pairs (pathway 1, Scheme 1a). Both routes lead to the same free energy of formation of the transition state (TS) from O_2(g) and *−* and also to the same rate equations. These direct or sequential O_2 dissociation steps are rendered irreversible by fast scavenging of O* by H* in later steps that are kinetically-insignificant; it is such steps that prevent the formation of O*-saturated surfaces and O* species to be present at coverages much lower than those of H* during catalysis in spite of thermodynamics that significantly favor O* over H*. These conclusions are consistent with those reached from mechanistic studies on bare Pt surfaces;[7,20−23] however, they cannot account for the alternate route made evident by the second term in eq 16, a term that, in contrast with the first term, does not depend on H_2 pressure.

At H_2 pressures above 20 kPa (and 603 K), the near-saturation coverages evident from independent H_2 uptake data[26] and the functional form of eq 15 dictate that the second route be mediated by a TS containing two O atoms and two H atoms in some form so as to give a second term in eq 15 that is independent of H_2 pressure (because H_2 pressures in the numerator and denominator must cancel). One plausible route involves a reaction of gaseous O_2 molecules (or weakly-bound O_2 analogues) with H*−H* pairs to form *HOOH*, a very reactive species that would cleave its O−O bond to form two OH* moieties or undergo intramolecular H-transfer and O−O dissociation to form H_2O* and O*,[67] either during the surface sojourn that forms H_2O_2 or after it desorbs and then readsorbs along the catalyst bed (pathway 2, Scheme 1b). The very reactive nature of H_2O_2 is evident from the very low temperatures (∼300 K) and specific solvents and additives that are required in order to inhibit its decomposition during on-purpose H_2O_2 synthesis from H_2−O_2 reactants.[68−73] At the higher temperatures used in our study, H_2O_2(g) decomposes (to H_2O and O_2) even via homogeneous routes (400−450 K)[74] or on nominally inert surfaces such as fused silica and borosilicate glass surfaces.[75,76]

The functional form of the second term in eq 15 may reflect instead the kinetic relevance of OH* recombination, with such species formed via preceding quasi-equilibrated steps (quasi-equilibrium denoted by oval symbols over double arrows) to form H_2O* and O*:

1. $O_2 + 2* \rightleftharpoons 2O*$ (K_{O_2})
2. $H_2 + 2* \rightleftharpoons 2H*$ (K_{H_2})
3. $O* + H* \rightleftharpoons OH* + *$ (K_{OH*})
4. $2OH* \longrightarrow H_2O* + O*$ (k_{H_2O*})

Such a hypothesis leads to a rate equation

$$r_{O_2,2} = K_{O_2} K_{H_2} K_{OH*} k_{H_2O*} [O_2][H_2]\theta_*^2 \tag{17}$$

which describes the functional form of the second term in eq 16, but only if H* is the MASI (i.e., $\theta_*^2 = K_{H_2}^{-1}[H_2]^{-1}$) and rates become independent of H_2 pressure. Equation 17 also acquires its functional form only when O* is in equilibrium with O_2 (and H_2 with H*), which would lead to surfaces nearly saturated with O* (i.e., $\theta_*^2 = K_{O_2}^{-1}[O_2]^{-1}$) at these conditions (as discussed in section 3.1) and to rates that would be independent of O_2 pressure and proportional to H_2 pressure. Such requirements contradict the observed kinetic trends (Figure 1).

These observations and assessments lead to the mechanistic proposal depicted as a sequence of elementary steps in Scheme 1, which gives, in turn, an equation for turnover rates:

$$r_{O_2} = K_{O_2} k_{O_2*-*} \theta_*^2 [O_2] + k_{O_2,H*-H*} \theta_{H*}^2 [O_2]$$
$$= \frac{K_{O_2} k_{O_2*-*} [O_2]}{(1 + \sqrt{K_{H_2}[H_2]})^2} + \frac{K_{H_2} k_{O_2,H*-H*} [H_2][O_2]}{(1 + \sqrt{K_{H_2}[H_2]})^2} \tag{18}$$

The first term contains the rate parameter for O_2 dissociation at *−* pairs ($K_{O_2}\, k_{O_2*-*}$) and a measure of the probability that such pairs can be found for a given value of θ_{H*} when H* species are randomly placed on surfaces through fast H_2 dissociation and H*−H* recombination steps. The second term accounts for contributions to turnover rates from reactions of O_2(g) (or weakly-bound O_2 molecules in equilibrium with O_2(g)) with H*−H* pairs. This term

https://doi.org/10.1021/acs.jpcc.2c08826
J. Phys. Chem. C 2023, 127, 4553−4569

contains the rate parameter for the formation of *HOOH* ($K_{O_2}\,k_{O_2,H^*-H^*}$ from O_2 and a H*−H* pair) and the probability that H*−H* pairs will be found at a given θ_{H^*} value. These values of θ_{H^*} and θ_* are given by independent measurements of H_2 uptakes on Pt nanoparticles at 473−673 K and a broad range of H_2 pressures (0.1−20 kPa of H_2);[26] these coverages represent those prevalent during H_2−O_2 reactions, as discussed earlier (section 3.1).

Measured H_2 oxidation rates (548−673 K; shown in Figure S1.3, SI), taken together with θ_{H^*} values derived from H_2 uptakes, were regressed to the functional form of eq 18 at each reaction temperature. The temperature dependences of $K_{O_2}k_{O_2*-*}$ and k_{O_2,H^*-H^*} (Figure 4) reflect the activation enthalpy

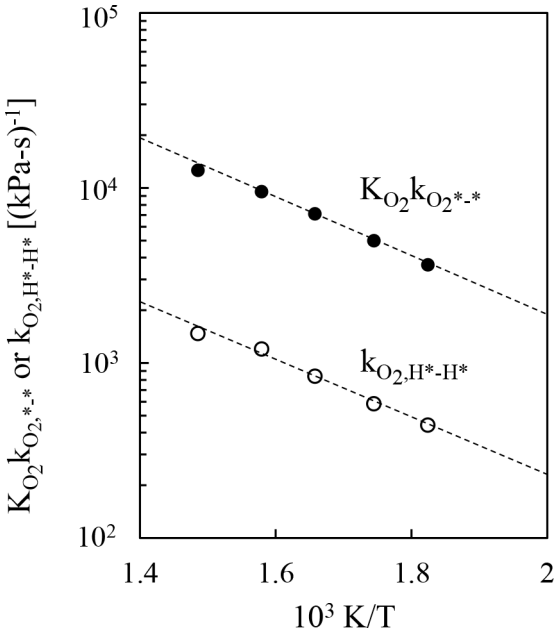

Figure 4. Arrhenius dependence of rate parameters ($K_{O_2}k_{O_2*-*}$, ●; k_{O_2,H^*-H^*}, ○) in H_2−O_2 reactions at 1−50 kPa H_2 and 1.5 kPa O_2 (0.2 wt % Pt/SiO_2, 2.3 nm mean cluster size).

and entropy for each O_2 activation route. The activation enthalpies are similar for these two routes (31 ± 2 and 31 ± 4 kJ mol^{-1}, respectively), a fortuitous coincidence that is confirmed from their respective DFT-derived enthalpies (sections 3.3 and 3.4). Measured pre-exponential factors for the rate parameters associated with O_2 dissociation on *−* pairs (3.1 (±0.1) × 10^8 bar^{-1} s^{-1}, Table 1) correspond to an entropy of activation of −88 ± 4 J mol^{-1} K^{-1}, a value that is significantly less negative than expected if the TS is immobile (from statistical mechanics methods; −236 J mol^{-1} K^{-1}) but similar to entropies estimated from heuristic guidance from desorption rate constants for weakly-bound species,[77] which posit the loss of one degree of translation upon adsorption (−99 J mol^{-1} K^{-1}). The pre-exponential factor for the rate parameter corresponding to O_2 with H*−H* pairs to form *HOOH* (3.8 (±0.2) × 10^7 bar^{-1} s^{-1}, Table 1) corresponds to an entropy of activation of −106 ± 7 J mol^{-1} K^{-1}, a value that is more negative than for direct O_2 dissociation (−88 ± 4 J mol^{-1} K^{-1}, Table 1). The formation of both TS structures involves a loss of translational entropy, but that for O_2 reactions with H*−H* also causes a loss of two-dimensional translation for the H* adlayer, which behaves essentially as a nonideal two-dimensional gas on Pt nanoparticles.[26] The formation of the four-centered *HOOH* TS (shown in section 3.4) causes each H* to lose some of its ∼35 J mol^{-1} K^{-1} entropy, derived from H_2 adsorption isotherms (473−673 K).[26] The activation enthalpies (31 ± 2 and 31 ± 4 kJ mol^{-1} for $K_{O_2}k_{O_2*-*}$ and k_{O_2,H^*-H^*}, respectively) and free energies (90 ± 3 and 102 ± 6 kJ mol^{-1}, respectively; 673 K) show that their different contributions to measured rates predominantly reflect their different activation entropies and the magnitude of the prevalent H_2 pressures and temperature, which determine the relative coverages of H* and *.

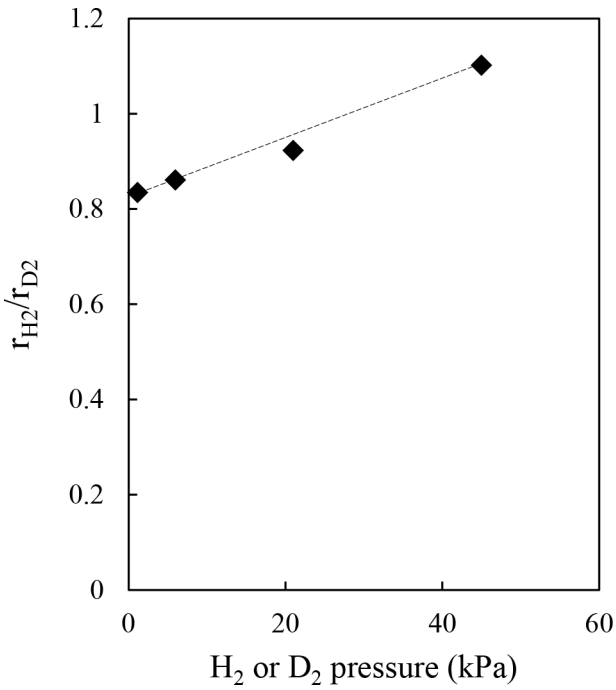

Figure 5. Ratio of rates for O_2 reactions with H_2 and D_2 (1.5 kPa O_2, 1−45 kPa H_2 or D_2, 603 K; 0.2 wt % Pt/SiO_2, 2.3 nm mean cluster size). The dashed line is shown to guide the eye and indicate trends.

Figure 5 shows that ratios of rates of O_2 reactions with H_2 and D_2 ($\chi = r_{H_2}/r_{D_2}$) are near unity at all H_2 (or D_2) pressures

Table 1. Kinetically Relevant Elementary Steps and Experimental Kinetic Parameters during H_2−O_2 Reactions on Pt/SiO_2 (0.2 wt % Pt/SiO_2, 2.3 nm Mean Cluster Size)

elementary step	rate constant	activation energy (kJ mol^{-1})[a]	pre-exponential factor (bar^{-1} s^{-1})[a]	activation entropy (J mol^{-1} K^{-1})[a]
O_2 + 2* → 2O*	$K_{O_2}k_{O_2*-*}$	31 ± 2	(3.1 ± 0.1) × 10^8	−88 ± 4
O_2 + 2H* → *HOOH*	k_{O_2,H^*-H^*}	31 ± 4	(3.8 ± 0.2) × 10^7	−106 ± 7

[a]Errors represent 95% confidence intervals from the regression analysis.

https://doi.org/10.1021/acs.jpcc.2c08826
J. Phys. Chem. C 2023, 127, 4553−4569

(2−45 kPa H_2 or D_2, 1.5 kPa O_2, 603 K) but show a slight monotonic increase over a very large (>20-fold) increase in H_2 pressure (0.8 at 2 kPa H_2; 1.1 at 45 kPa H_2). H_2 oxidation turnover rates reflect the combined contributions from the two terms in eq 18; consequently, these rate ratios reflect the combined kinetic isotope effects (KIEs) for both relevant rate constants ($k_{O_2,*-*}$ and $k_{O_2,H*-H*}$), as well as the thermodynamic isotope effects (TIEs) for dissociative H_2 adsorption (K_{H_2}) and molecular O_2 adsorption (K_{O_2}). TIE values for K_{H_2} on Pt nanoparticles are near unity, as evident from H_2 and D_2 chemisorption isotherms measured on Pt/SiO_2 catalysts that are nearly identical (TIE = 1.0 at $\theta_{H*/D*}$ = 0.8, TIE = 0.9 at $\theta_{H*/D*}$ = 0.7; 623 K).[78] Values for θ_{D*} at a given D_2 pressure are therefore similar to θ_{H*} values at the same H_2 pressure and can be obtained independently from H_2 uptakes, as discussed in section 3.1. The H_2−O_2 and D_2−O_2 rate data shown in Figure 5, taken together with these θ_{H*} and θ_{D*} values, were regressed to the functional form of eq 18 to extract the values of the KIE for each parameter ($k_{O_2,H*-H*}$ and $K_{O_2}k_{O_2*-*}$). The KIE values obtained for both parameters are near unity (KIE for $k_{O_2,H*-H*}$ = 1.1 ± 0.1, and KIE for $K_{O_2}k_{O_2*-*}$ = 0.8 ± 0.1). These KIE values for $k_{O_2,H*-H*}$ reflect a TS that occurs very early (Pt−H* bonds nearly intact and O−H* bonds not yet formed, as shown in section 3.4) or a very late TS (Pt−H* nearly cleaved and O−H* nearly formed) along the reaction coordinate. The KIE for O_2 dissociation and TIE for molecular O_2 adsorption, the product of which reflects the KIE for $K_{O_2}k_{O_2*-*}$, are expected to be unity given the lack of involvement of H_2/D_2-derived species in the formation of the TS. The near-unity KIE values are consistent with those obtained from DFT assessments (shown in section 3.4) and with the expectations from the proposed mechanism.

3.3. Theoretical Assessments of O_2 Dissociation Steps on Vicinal Bare Pt Atoms (Pathway 1). O_2 dissociation to form O* occurs on ensembles of bare Pt atoms that stochastically appear within H* adlayers as a result of quasi-equilibrated H_2 dissociation steps during H_2−O_2 reactions; it is one of the kinetically-relevant steps involved in the ultimate formation of the stable H_2O products. Such steps also mediate CH_4,[24] C_2H_6,[25] and CO[24] reactions with O_2 on Pt surfaces, albeit in the presence of coadsorbates that differ in identity and coverage from those in the present study (θ_{H*} = 0.7−1.2, section 3.1). On the sparsely-covered surfaces that prevail during CH_4−O_2[24] and C_2H_6−O_2[25] reactions, O_2 dissociation was shown experimentally to be essentially barrierless (3 kJ mol^{-1}) while DFT-derived O_2 dissociation barriers were about 20 kJ mol^{-1} on Pt_{201} nanoparticles;[24] in both cases, activation barriers are smaller than those reported here (31 ± 2 kJ mol^{-1}, Table 1) on Pt nanoparticle surfaces at high H* coverages. DFT treatments show that O_2 dissociation occurs via the quasi-equilibrated formation of weakly-bound O_2* followed by its reaction with a vicinal * to form an O*−O* pair,[24,25] as shown in the steps below:

$$1.\quad O_2 + * \rightleftharpoons O_2^* \qquad (K_{O_2})$$

$$2.\quad O_2^* + * \longrightarrow 2O^* \qquad (k_{O_2^*-*})$$

The O_2 dissociation barrier (referenced to gaseous O_2) is thus defined as the sum of the molecular O_2 adsorption enthalpy (step 1) and the barrier of the formation of two O* from molecularly adsorbed O_2* (step 2).

DFT-derived enthalpies of gaseous and bound species (O_2, O_2*, and O*) and of TS structures for the molecular and dissociative adsorption of O_2 were calculated on bare Pt(111) surfaces (Figure 6) and also on H*-saturated Pt(111) surfaces from which different numbers of H* atoms were removed to form ensembles of bare Pt atoms of different sizes (Table 2 and Figure 9). The binding of O_2 molecules involves a triplet-to-singlet transition to form O_2* bound in an η_2 di-σ configuration on a bare Pt(111) plane; this step has a reaction enthalpy of −53 kJ mol^{-1} (603 K, Figure 6), which resembles DFT-derived O_2* formation electronic energies reported earlier on (111) facets of bare Pt nanoparticles (−54 kJ mol^{-1}, Pt_{201}).[24] O_2* can dissociate to form O*−O* pairs with O atoms at 3-fold hollow fcc sites (shown in Figure 7c) or at two vicinal 3-fold hollow hcp sites (shown in Figure 7e). Such steps are very exothermic (−137 kJ mol^{-1} for the 3-fold fcc binding mode and −77 kJ mol^{-1} for the 3-fold hcp binding mode, 603 K; Figure 6).

The minimum-energy path (MEP) for O_2* dissociation involves the shift of one O atom to a bridge site and the other one to an atop site as the TS for O−O cleavage incipiently forms; the two O* atoms that form bind at vicinal 3-fold hollow sites (Figure 7). These O* species are much more stable when bound at 3-fold fcc sites instead of 3-fold hcp sites (by 60 kJ mol^{-1}), yet dissociation barriers are actually smaller (by 10 kJ mol^{-1}) for O* species bound at 3-fold hcp sites (referenced to the same O_2* reactant state, Figure 6), even though Brønsted−Evans−Polanyi scaling relations would lead to barriers that decrease as products formed from a common precursor become more stable.[79] Such findings illustrate the imperfections that plague scaling relations when binding of the TS and product occurs at separate sites.

For O_2* dissociation steps that form O* bound at 3-fold fcc sites, the O−O bond involves the lengthening of the O−O bond from 0.137 nm in O_2* (Figure 7a) to 0.191 nm at the TS (Figure 7b), which is centered at a 3-fold hcp site; this 3-fold hcp site is located between the two 3-fold fcc sites that ultimately bind the O* products (Figure 7c). The TS for O_2* dissociation steps of O_2* that form O* bound at 3-fold hcp sites is likewise centered on top of the 3-fold fcc site that lies between the binding locations for the two O* atoms that form as products (Figure 7d,e); it has a longer O−O bond than for the TS that places the O atoms at 3-fold fcc sites (0.230 vs 0.191 nm), indicative of a "later" TS along the O−O cleavage reaction coordinate. The deviations from the expectations of scaling relations reflect the tendency for 3-fold hollow fcc sites to bind adsorbates more strongly than 3-fold hcp sites and the unique positioning of the TS in between the product binding sites (e.g., TS for dissociation into 3-fold fcc sites is bound to a 3-fold hcp site and TS for dissociation into 3-fold hcp sites is bound to a 3-fold fcc site). Scaling relations may fail for TS structures that require concerted interactions with spatially separate binding points, as is usually the case in dissociation reactions; in such cases, the inability of the TS to maintain contact with stable binding points prevents the TS from benefiting from a more stable product state that cannot be accessed geometrically as the TS forms.

On sparsely-covered Pt(111) surfaces, the enthalpic barriers for O_2* dissociation to form O* products at 3-fold fcc and hcp locations (50 kJ mol^{-1} and 40 kJ mol^{-1}, respectively) and for O_2* desorption (53 kJ mol^{-1}) are similar, leading to values of

https://doi.org/10.1021/acs.jpcc.2c08826
J. Phys. Chem. C 2023, 127, 4553−4569

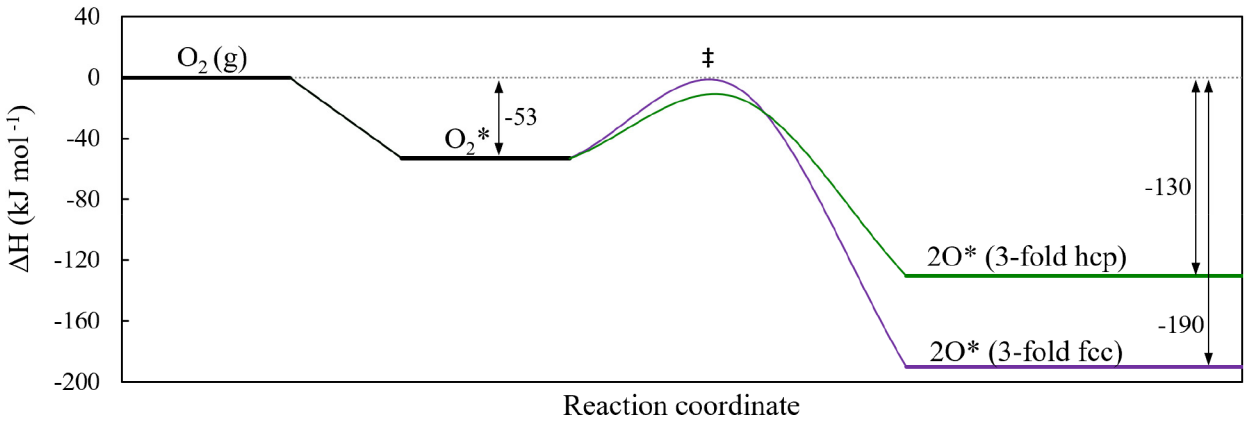

Figure 6. DFT-derived reaction enthalpy diagram for O_2 adsorption and dissociation into 3-fold hollow sites on a bare Pt(111) plane at 603 K (PW91).

Table 2. DFT-Derived Molecular and Dissociative O_2 Adsorption Enthalpies (Referenced to O_2(g)) on H*-Covered Pt Surfaces Derived from DFT (PW91)

H* binding mode	Pt ensemble size (no. of H* vacancies)	molecular O_2 adsorption enthalpy (kJ mol^{-1})[a]	dissociative O_2 adsorption enthalpy (kJ mol^{-1})[a,b]
	∞	−53	−190
3-fold fcc	6	−31	−100
	5	−21	−88
	4	−9	−76
	3	−6	−60
	2	30	−38
atop	6	−45	−157
	5	−39	−156
	4	−38	−114
	3	−39	−69
	2	−29	−23

[a]603 K. [b]Dissociation into the 3-fold fcc binding site.

nearly zero for the enthalpy of formation of two O* from one O_2(g) on such surfaces. These barriers and binding energies can be influenced, however, by the identity and coverage of any coadsorbed species,[24,80] in this case H*. O_2 dissociation barriers (from DFT-derived electronic energies) are significantly larger on Pt(111) surfaces with 0.67 ML of CO* (101 kJ mol^{-1}, 0 K)[80] and Pt_{201} clusters with 0.99 ML of O* (207 kJ mol^{-1}, 0 K)[24] than on bare Pt(111) surfaces (−3 kJ mol^{-1}, 603 K; Figure 6) because through-surface and through-space repulsion is stronger for species that are larger and more electron-rich than H*.

DFT-derived enthalpies for the formation and dissociation of O_2* (Table 2) and for its TS are examined next through the systematic removal of a different number of vicinal H* from Pt(111) surfaces initially containing 1 ML of H*; these methods are used to assess how the size of bare Pt ensembles (exposed upon H* removal) influences the energies relevant to O_2 activation routes. The 3-fold fcc (Figure 8a) and atop (Figure 8b) H* binding positions are chosen for these comparisons because they represent the most stable H* binding configurations on Pt(111) surfaces.[26] The number of H* atoms removed serves to define the size of a bare Pt ensemble, and it influences O_2* binding and dissociation enthalpies (as shown in Table 2). Varying the ensemble size also brings about a concomitant change in H* coverage, the effects of which cannot be separated from the effects of ensemble size given the system size (4 × 4 periodic supercells, 16 H* on the Pt (111) plane at 1 ML H*; section 2.3). Such changes in H* coverage with ensemble size illustrate one of the limitations of finite models in capturing these phenomena, in this case amplifying the apparent effect of ensemble size on O_2 adsorption and dissociation enthalpies. This DFT treatment also fails to capture the inherent mobility of H* at relevant catalytic temperatures, where it nominally behaves as a two-dimensional gas,[26] and the lateral relaxation of H* adlayers that occurs on curved nanoparticle surfaces. Repulsive interactions among adsorbates tend to be weaker on nanoparticles than on extended flat surfaces because of curvature and lateral relaxation; for instance, the binding of CO* at spaces within CO* adlayers at (111) facets in Pt_{201} nanoparticles is much stronger than on extended Pt(111) planes (79 vs 7 kJ mol^{-1} heat of adsorption) because lateral relaxation effects lengthen CO*−CO* distances and weaken repulsive interactions.[80] Thus, DFT energy estimates modeled on extended planar Pt(111) surfaces give less negative adsorption energies and higher barriers for O_2 dissociation than those expected on realistic curved Pt surfaces; such overpredictions are greater on smaller bare Pt ensembles as a result of the high concomitant H* coverages and stronger repulsive interactions within the rigid adlayers imposed by the periodicity of the system.

O_2* formation from O_2(g) becomes less exothermic (and ultimately endothermic) as bare Pt ensembles become smaller or the H* coverages increase, indicative of its greater discomfort as adlayers become denser (locally or globally); for instance, the molecular O_2 adsorption enthalpy is −53 kJ mol^{-1} on an infinite Pt ensemble (equivalent to a bare Pt(111) surface) and +30 kJ mol^{-1} on an ensemble size of two vacancies within H* adlayers in 3-fold fcc binding mode (equivalent to 7/8 ML of H* modeled in a 4 × 4 periodic lattice) (603 K; Table 2). O_2 dissociation enthalpies of the O_2 ions (from O_2(g)) also become less negative on smaller Pt ensembles (−190 kJ mol^{-1} on an infinite Pt ensemble; −38 kJ mol^{-1} on an ensemble size of two Pt atoms within H* adlayers in 3-fold fcc binding mode, 603 K; Table 2). Similar trends are evident when H* is placed in atop binding locations on Pt(111) surfaces using the same PW91 functional (Table 2) or when H* is placed at 3-fold fcc binding locations and another functional is used (RPBE, section S2.2 in the Supporting Information). Through-space and through-surface interactions

https://doi.org/10.1021/acs.jpcc.2c08826
J. Phys. Chem. C 2023, 127, 4553−4569

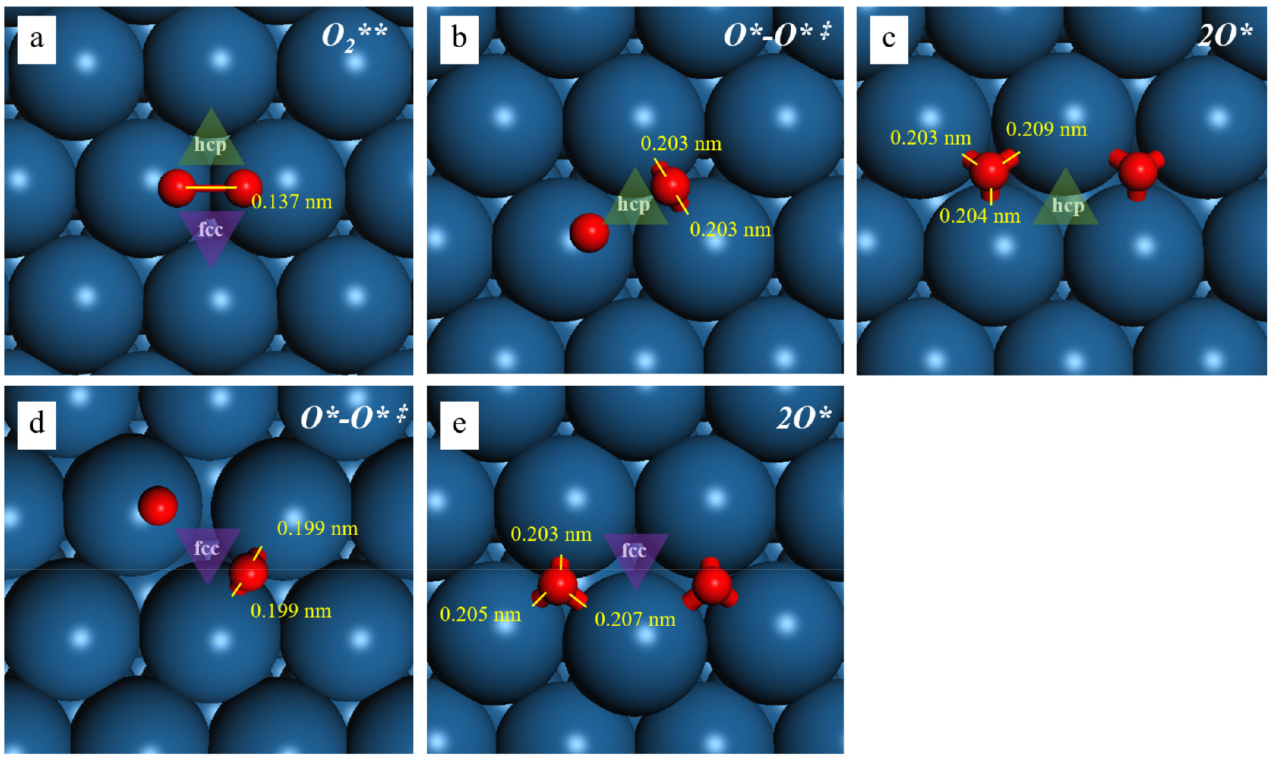

Figure 7. DFT-derived structures for O_2* (a), TS (b), and two O* (c) for the elementary step involving the dissociation of O_2* to form two O* at 3-fold fcc sites. TS (d) and O*−O* products (e) for the formation of two O* at 3-fold hcp sites on bare Pt(111) surfaces (PW91).

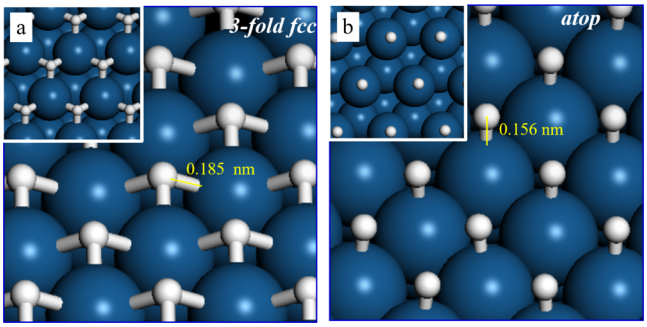

Figure 8. Pt(111) planes covered with 1 ML of H* in 3-fold fcc (a) and at atop (b) binding locations (PW91).

of O_2* species with the H* adlayer also influence the structure and stability of the O_2* dissociation TS, which determines the magnitude of the measured values of $K_{O_2}k_{O_2*-*}$. Larger vacant ensembles, whether formed by removing vicinal H* atoms from a surface at 1 ML or by decreasing H* coverages throughout the surface, bind TS structures more strongly (Figure 9), leading to O_2 dissociation barriers (referenced to O_2(g)) that decrease from 95 kJ mol^{-1} on two-atom ensembles to 32 kJ mol^{-1} on six-atom ensembles and ultimately to −3 kJ mol^{-1} (Figure 6) on bare Pt(111) surfaces (603 K).

The effects of the size of the bare Pt ensemble on O_2 dissociation barriers indicate that O_2 dissociation rates ($r_{O_2,1}$) cannot be rigorously described by Langmuirian treatments, even when H* coverages in eq 18 are obtained independently and used to describe the effects of repulsion on H* binding energies. These O_2 dissociation rates reflect instead the combined contributions from all possible ensembles of bare Pt atom sites present at any given H* coverage

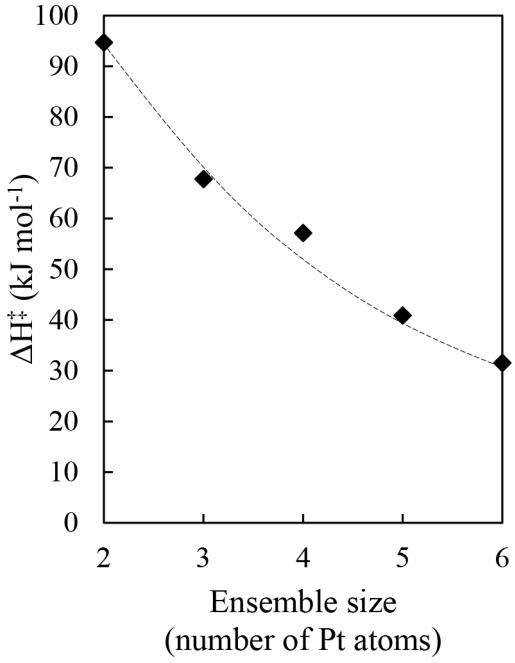

Figure 9. Effect of Pt ensemble size on enthalpy barriers for O_2 dissociation into 3-fold hollow fcc sites, relative to gas-phase O_2 and the Pt(111) plane with coadsorbed H* in 3-fold fcc binding mode on the Pt(111) plane at 603 K (PW91). The dashed curve is shown to guide the eye and indicate trends.

$$r_{O_2,1} = \sum_i K_{O_2,i} k_{O_2*-*,i} \theta_*^i [O_2] \tag{19}$$

where i denotes the number of contiguous bare Pt atoms in an ensemble, θ_* is the fractional coverage of bare sites, and

https://doi.org/10.1021/acs.jpcc.2c08826
J. Phys. Chem. C 2023, 127, 4553−4569

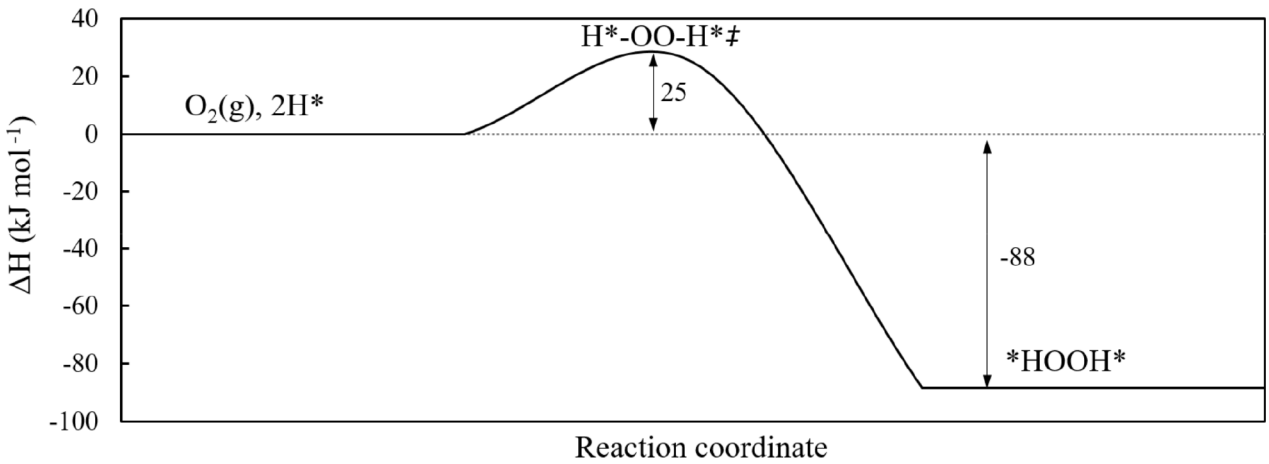

Figure 10. DFT-derived reaction enthalpy diagram for the reaction of O_2 with H*−H* (3-fold fcc binding location) to form *HOOH* on an H*-saturated Pt(111) plane at 603 K (PW91).

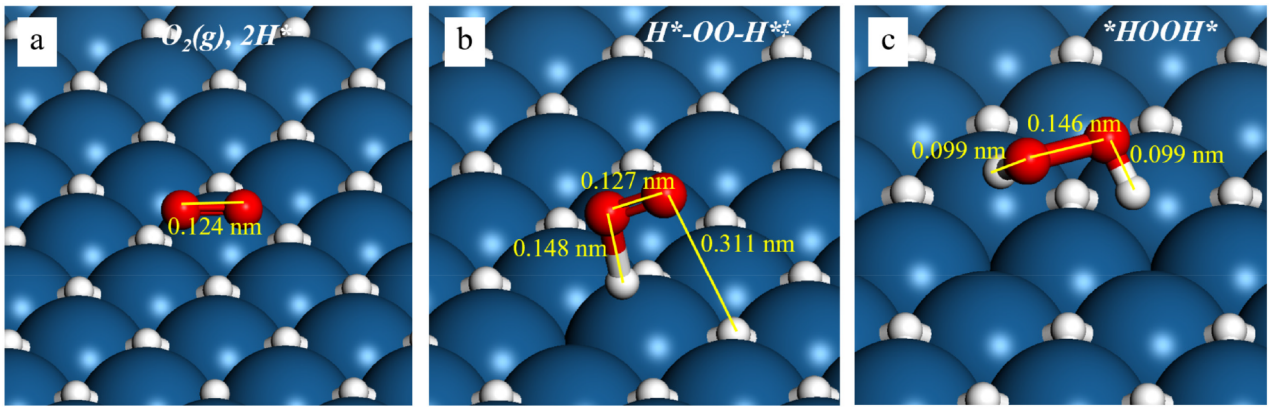

Figure 11. Structures of a reactant (a), transition state (b), and product (c) for *HOOH* formation on an H*-covered Pt(111) plane with H* in 3-fold fcc binding mode (PW91).

$K_{O_2,i}k_{O_2*-*,i}$ is the O_2 dissociation rate constant on an ensemble with i atoms for H* and * randomly positioned at surfaces through rapid quasi-equilibrated H_2 dissociation−recombination events. Each i-atom ensemble contributes to the O_2 dissociation rates according to its prevalence at a given H* coverage and the respective rate constants, given by the free energy of formation of the TS structure (O*−O*‡):

$$K_{O_2,i}k_{O_2*-*,i} = \frac{k_B T}{h} e^{\left(-\frac{\Delta G_i^{\ddagger}}{k_B T}\right)} = \frac{k_B T}{h} e^{\left(-\frac{\Delta H_i^{\ddagger} - T\Delta S_i^{\ddagger}}{k_B T}\right)} \tag{20}$$

Here, $\Delta G_i^{\ddagger}$, $\Delta H_i^{\ddagger}$, and $\Delta S_i^{\ddagger}$ represent the free energy, enthalpy, and entropy of formation of the TS*−O*‡ on a site ensemble with i bare sites from one O_2(g) molecule. Larger ensembles give lower $\Delta H_i^{\ddagger}$ barriers (Figure 9) than smaller ensembles, but such trends are compensated for by a smaller value for $\theta_*^{\,i}$ (eq 19), which accounts for the probability of encountering large ensembles of a given size i. Yet, Langmuirian treatments are able to adequately describe H_2−O_2 rates on surfaces containing significant H* coverages because such averaging may lead to predominant contributions by ensembles of a given intermediate size and reactivity but also because of the "forgiving" functional form of Langmuirian adsorption and rate equations; in practice, the trends imposed by these equations are visually reinforced by their clear asymptotic limits at high and low coverages, with few rate or uptake measurements at the intermediate coverages where their effects are most evident.[26]

3.4. Theoretical Assessments of O_2 Reactions with Vicinal H*−H* Pairs (Pathway 2). Direct reactions of O_2(g) with H*−H* pairs represent the route described by the second term in eq 18. Its rate constant (k_{O_2,H^*-H^*}) reflects the free energy of formation of a TS in which O_2(g) interacts in a concerted manner with H*−H* pairs on surfaces densely covered with H*. DFT-derived enthalpies of reactants, transition states, and products are described here for the formation of *HOOH* products on Pt(111) surfaces covered by 1 ML of H* with H* species placed at their most stable binding locations (3-fold fcc and atop).

Figure 10 shows the reaction enthalpy diagram, and Figure 11 shows reactant, TS, and product structures for O_2 reactions with H*−H* pairs for the case of H* atoms at 3-fold fcc sites. The TS for this elementary step (Figure 11b) involves predominant interactions of O_2 with only one of the two H* atoms, indicative of a sequential process by which the two vicinal H* atoms react with O_2. One H* shifts from its 3-fold fcc position to an atop position to form an incipient bond with one O atom (O−H bond length of 0.148 nm vs 0.099 nm in *HOOH*), while the other H* remains essentially unaffected. The O_2 moiety at the TS retains the triplet configuration of O_2(g), whereas the product *HOOH* is in the singlet state; the O−O bond length in the TS (0.127 nm) becomes slightly

https://doi.org/10.1021/acs.jpcc.2c08826
J. Phys. Chem. C 2023, 127, 4553−4569

longer than in O_2(g) (0.124 nm, Figure 11a) but remains much shorter than in the product state (0.146 nm, Figure 11c). The early nature of this TS is consistent with the near-unity KIE values calculated from DFT for this step (1.2, 603 K; Table 3) and measured KIE (1.1 ± 0.1, 603 K; section 3.2) on surfaces nearly saturated with H*. The DFT-derived enthalpy barrier (25 kJ mol^{-1}, 603 K; Figure 10) is similar to the measured activation barriers (31 ± 4 kJ mol^{-1}, section 3.2). The activation barriers obtained using the RPBE functional (27 kJ mol^{-1} for H* at 3-fold fcc sites, 603 K; Supporting Information S2.4) are similar to those calculated with PW91 functionals.

Table 3. DFT-Derived Activation Barriers and Kinetic Isotope Effects for the Reaction of O_2 with H*−H* on an H*-Covered Pt(111) Plane (PW91, 603 K)

H* binding mode	activation barrier for *HOOH* formation (kJ mol^{-1})	reaction enthalpy for *HOOH* formation (kJ mol^{-1})	kinetic isotope effect for *HOOH* formation
3-fold fcc	25	−88	1.2
atop	4	−101	1.4

Repulsion among H* species on extended Pt(111) planes covered by 1 ML of H* is stronger than on Pt nanoparticles because of the rigid periodic boundaries that define supercells (as discussed in section 3.3), leading to H* that is less stable and thus more reactive. These effects, however, are likely to be weak because the early TS does not lead to significant perturbations of the M−H bonds. DFT-derived enthalpies were not calculated as a function of H* coverage because of this, but H* species are expected to become more reactive in reactions with O_2(g) as the H* coverage increases.

Figure 12 shows reactant, TS, and product structures for O_2 reactions with H*−H* pairs at atop instead of 3-fold fcc locations. In contrast with H*−H* pairs at 3-fold fcc sites (Figure 11), O_2 reactions with H*−H* at atop sites are mediated by more symmetrical TS structures (Figure 12b), indicative of the concerted addition of two H* atoms to the two O atoms in O_2. Its reactant-like character is evident from its two O−H bonds, which are significantly longer at the TS than in the *HOOH* products (0.163 and 0.180 nm at the TS, Figure 12b; 0.099 and 0.099 nm in *HOOH*, Figure 12c). The O−O bond at the TS (0.127 nm, Figure 12b) is similar to that in O_2(g) (0.124 nm, Figure 12a) and significantly shorter than that in *HOOH* (0.146 nm, Figure 12c), while the O_2 moiety retains the triplet configuration, as in the case of the TS formed from H*−H* pairs at 3-fold fcc binding locations. The DFT-derived KIE values are also near unity in this case but slightly larger than at 3-fold fcc H* sites (1.4 for atop H* vs 1.2 for 3-fold fcc H*, 603 K; Table 3); the enthalpic barriers are smaller for H* species at atop locations (4 kJ mol^{-1} for atop H* vs 25 kJ mol^{-1} for 3-fold fcc H*, 603 K; Table 3), consistent with weaker M−H bonds at atop than at 3-fold fcc sites. The weaker binding of H* in atop configurations also leads to their less prevalent presence during H_2−O_2 reactions and to a compensation between its higher reactivity and lower coverages (free energies of adsorption: 30 kJ mol^{-1} for 3-fold fcc, 32 kJ mol^{-1} for atop H*; 1/2 ML of H*, 593 K).[26] The low *HOOH* formation activation barriers and KIE values near unity for *HOOH* formation from these DFT methods are consistent with measurements (section 3.2) and support the mechanistic conclusions inferred from the observed kinetic trends in O_2 and H_2 pressure.

3.5. Effects of Pt Nanoparticle Size on H_2 Oxidation Turnover Rates. H_2 oxidation turnover rates were also measured on Pt/SiO_2 catalysts with different dispersions and nanoparticle diameters (1.7, 2.3, and 6.2 nm mean diameters; Figure 13). Turnover rates vary less than two-fold, and kinetic trends were similar on all samples, in spite of a size range that leads to significant differences in the average coordination of exposed Pt atoms.[38] Table 4 shows measured rate constants for O_2 dissociation ($K_{O_2}k_{O_2*-*}$) and reaction with H*−H* pairs ($k_{O_2,H*-H*}$), derived by regressing the H_2−O_2 rate data in Figure 13 to the functional form of eq 18; in such estimates, H* binding energies are assumed to depend weakly on surface coordination, as evident from H_2 uptakes measured on Pt particles of varying size (1.6−9.1 nm),[26] so that θ_{H*} values for 3 nm particles (used in the regressions shown in section 3.1) remain accurate for the other samples. Such weak effects of surface coordination on reactivity for H_2 oxidation are likely to reflect, in part, the relative structure insensitivity of H* binding[26] compared to the binding of other adsorbates (e.g., CO* and O*) and the softening of site location effects on binding energies by H* adlayers that place more H* near the undercoordinated metal atoms at the corners and edges of Pt nanoparticles.[29]

The values of $K_{O_2}k_{O_2*-*}$ (pathway 1) increased slightly with increasing particle size; $K_{O_2}k_{O_2*-*}$ values were 1.7 times larger

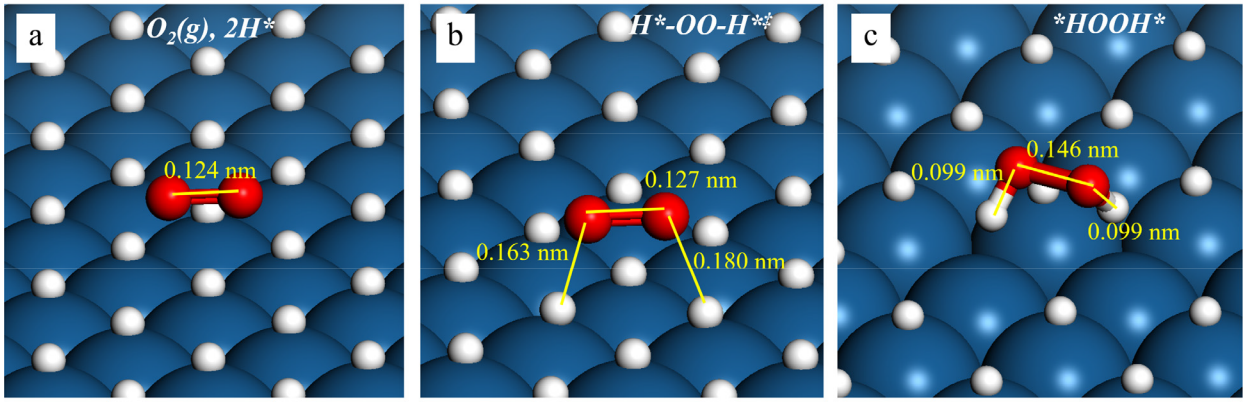

Figure 12. Structures of reactant (a), transition state (b), and product (c) for *HOOH* formation on a H*-covered Pt(111) plane with H* in atop binding mode (PW91).

https://doi.org/10.1021/acs.jpcc.2c08826
J. Phys. Chem. C 2023, 127, 4553−4569

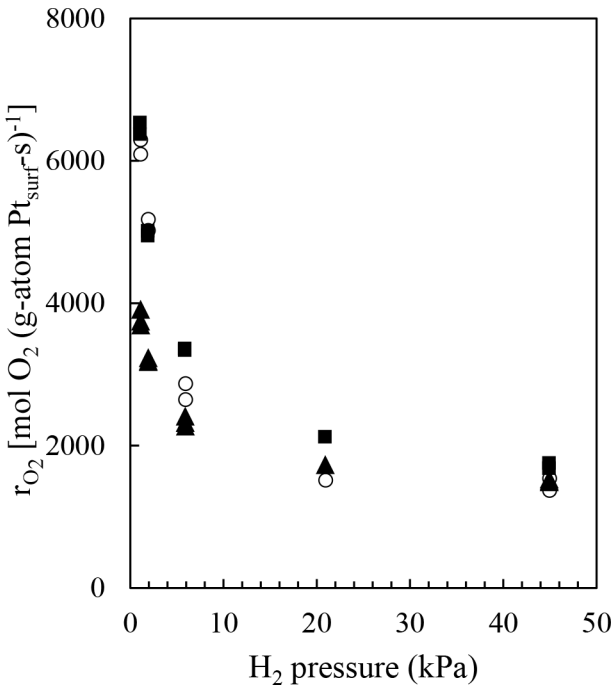

Figure 13. H_2 oxidation turnover rates on supported Pt particles of different sizes (6.2 (■), 2.3 (○), and 1.7 nm (▲)) at 1.5 kPa O_2 and 603 K.

Table 4. Effects of Average Pt Nanoparticle Size on Rate Constants for H_2−O_2 Reactions at 603 K (1−45 kPa H_2, 1.5 kPa O_2)

mean particle size (nm)	$K_{O_2}k_{O_2*-*}$ (kPa^{-1} s^{-1})[a]	$k_{O_2,H*-H*}$ (kPa^{-1} s^{-1})[a]
1.7	4900 (±200)	790 (±20)
2.3	8100 (±300)	630 (±20)
6.2	8400 (±300)	880 (±30)

[a]Errors represent 95% confidence intervals from the regression analysis.

on 6.2 nm than on 1.7 nm nanoparticles (Table 4). These trends are consistent with those measured on bare Pt surfaces during CH_4−O_2 reactions, which increased slightly with increasing nanoparticle diameter, albeit at higher temperatures than those in the present study (O_2 dissociation rate parameter is 2200 kPa^{-1} s^{-1} on 1.8 nm Pt particles vs 2800 kPa^{-1} s^{-1} on 8.5 nm Pt particles; 873 K).[24] The effects of Pt nanoparticle diameter on the rates of O_2 dissociation may reflect the decoration of minority low-coordination Pt atoms at edges and corners by strongly bound O* or OH* species, thus rendering them inaccessible for catalytic turnovers. Such atoms become more prevalent as Pt nanoparticles decrease in size, thus possibly accounting for the slightly lower turnover rates on the smaller Pt nanoparticles. Similar decoration effects, with weak consequences for turnover rates, have also been reported for other reactions (e.g., CO hydrogenation, CO oxidation, and CO_2 hydrogenation), for which strongly bound CO*, C*, or O* species caused lower rates on smaller particles.[59,60,81,82] The effect of particle size on H_2 oxidation turnover rates becomes even less pronounced with increasing H_2 pressure and H* coverage (Figure 13); these higher H* coverages may weaken the binding of decorating species, thus decreasing their effects. The rate constant for the reaction of O_2(g) with H* pairs ($k_{O_2,H*-H*}$, pathway 2) remained nearly constant as the particle size was varied (790 ± 20 kPa^{-1} s^{-1} on 1.7 nm particles vs 880 ± 30 kPa^{-1} s^{-1} on 6.2 nm particles; Table 4). The absence of any dependence of $k_{O_2,H*-H*}$ values on particle size also reflects the early nature of the *HOOH*‡ TS structure that mediates the kinetically-relevant step for this pathway (section 3.4). The *HOOH*‡ TS contains O−O and O−H bonds that are nearly unperturbed from their reactant state, and thus the TS can only weakly sense the binding properties of surface H*, which do not depend strongly on surface coordination. The early TS and partial erasure of site location effects by H* adlayers render the inherent nonuniformity of Pt surfaces inconsequential in H_2−O_2 reactions despite the contrast with strict Langmuirian requirements of site equivalency.

4. CONCLUSIONS

In this study, the elementary steps for the reaction of H_2 and O_2 to form H_2O on Pt nanoparticles at moderate temperatures (500−700 K) and suprastoichiometric reductant/oxidant ratios (H_2/O_2 molar ratios >2) were elucidated through a combination of kinetic and isotopic data and theoretical treatments on Pt(111) surfaces. H_2 oxidation rates on Pt nanoparticles predominantly covered by H* are mediated by direct reactions of gaseous O_2 with catalytic surfaces, which occur via two kinetically-relevant pathways: (i) O_2 dissociation on an ensemble of bare Pt atoms to form two adsorbed O atoms and (ii) the O_2 reaction with H*−H* pairs to form *HOOH*, which decomposes rapidly in subsequent steps. The relative contributions of each pathway to measured reaction rates are driven by differences in their respective activation entropies and the prevalent coverage of H*, which are formed via quasi-equilibrated H_2 dissociation steps and are thus present at coverages that can be rigorously determined from independent measurements of H_2 uptake.

O_2 dissociation barriers decrease as the size of the landing ensemble increases, as a result of the stronger binding of the O*−O*‡ TS on larger ensembles; such an effect is compensated for by the lower probability of O_2(g) colliding with large ensembles on surfaces that are mostly covered by H* (θ_{H*} ranging from 0.7 to 1.2), leading to contributions by ensembles of varying size that depend on prevalent H* coverages. These findings render traditional Langmuirian treatments only approximate in their ability to describe these surface reactions and underscore the importance of evaluating the effects of coadsorbates in instances where they impact the energies of the kinetically-relevant transition states and their relevant precursors differently. Despite these challenges, Langmuirian treatments are still able to adequately describe H_2 oxidation rate data over a range of H* coverages due in part to our ability to determine such coverages independently from H_2 chemisorption isotherms and also to the versatility of the form of Langmuirian adsorption and rate equations.

■ ASSOCIATED CONTENT

Supporting Information

The Supporting Information is available free of charge at https://pubs.acs.org/doi/10.1021/acs.jpcc.2c08826.

Additional experimental work and density functional theory calculations (PDF)

https://doi.org/10.1021/acs.jpcc.2c08826
J. Phys. Chem. C 2023, 127, 4553−4569

AUTHOR INFORMATION

Corresponding Author

Enrique Iglesia − *Department of Chemical Engineering, University of California at Berkeley, Berkeley, California 94720, United States*; orcid.org/0000-0003-4109-1001; Email: iglesia@berkeley.edu

Author

Haefa Mansour − *Department of Chemical Engineering, University of California at Berkeley, Berkeley, California 94720, United States*

Complete contact information is available at: https://pubs.acs.org/10.1021/acs.jpcc.2c08826

Notes

The authors declare no competing financial interest.

ACKNOWLEDGMENTS

We acknowledge financial support from the National Science Foundation for a Graduate Research Fellowship for H.M. and from the BP p.l.c. for funding all research activities required for the contents of this manuscript and specifically for access to computational resources at BP High Performance Computing. Technical discussions with Dr. Eric Doskocil are also gratefully acknowledged. We also thank Dr. Wenshuo Hu for his proofreading of the manuscript.

REFERENCES

(1) Davy, H. Neue Versuche Und Bemerkungen Über Das Verbrennen von Gasförmigen Mengungen. *Ann. Phys.* **1817**, *56*, 242−255.

(2) Döbereiner, J. W. Proprietes Nouvelles et Remarquables Reconnues Au Sous-Oxide de Platine, Au Sulfure Oxide Ey a La Poussiere de Meme Metal. *Ann. Chim. Phys.* **1823**, *24*, 91−96.

(3) Faraday, M. Siebente Reihe von Experimental-Untersuchungen Über Elektricität. *Ann. Phys.* **1834**, *109*, 481−520.

(4) Boreskov, G. K. Catalytic Activation of Dioxygen. *Catalysis* **1982**, *3*, 39−137.

(5) Hanson, F. V.; Boudart, M. The Reaction between H_2 and O_2 over Supported Platinum Catalysts. *J. Catal.* **1978**, *53*, 56−67.

(6) Michaelides, A.; Hu, P. Catalytic Water Formation on Platinum: A First-Principles Study. *J. Am. Chem. Soc.* **2001**, *123*, 4235−4242.

(7) Yang, M. L.; Fan, C.; Zhu, Y. A.; Sui, Z. J.; Zhou, X. G.; Chen, D. Selective Oxidation of Hydrogen in the Presence of Propylene over Pt-Based Core-Shell Nanocatalysts. *J. Phys. Chem. C* **2015**, *119*, 21386−21394.

(8) Boudart, M.; Collins, D. M.; Hanson, F. V.; Spicer, W. E. Reactions between H_2 and O_2 on Pt at Low and High Pressures: A Comparison. *J. Vac. Sci. Technol.* **1977**, *14*, 441−443.

(9) Meitzner, G. D.; Iglesia, E.; Baumgartner, J. E.; Huang, E. S. The Chemical State of Gallium in Working Alkane Dehydrocyclodimerization Catalysts. In Situ Gallium K-Edge X-Ray Absorption Spectroscopy. *J. Catal.* **1993**, *140*, 209−225.

(10) Tsai, P. K.; Maple, M. B. Oscillatory Oxidation of H_2 over a Pt Catalyst. *J. Catal.* **1986**, *101*, 142−152.

(11) Zuniga, J. E.; Luss, D. Kinetic Oscillations during the Isothermal Oxidation of Hydrogen on Platinum Wires. *J. Catal.* **1978**, *53*, 312−320.

(12) Boreskov, G. K.; Slin'ko, M. G.; Chesalova, V. S. *Zh. Fiz. Khim.* **1956**, *30*, 2787.

(13) Mansour, H. *Scavenging of H_2 with O_2 and CO_2 on Noble Metal Nanoparticles: Mechanistic Insights and Coupling with Dehydrogenation Reactions*; University of California, Berkeley, 2020.

(14) Kaneko, S.; Arakawa, T.; Ohshima, M.-a.; Kurokawa, H.; Miura, H. Dehydrogenation of Propane Combined with Selective Hydrogen Combustion over Pt-Sn Bimetallic Catalysts. *Appl. Catal. A Gen.* **2009**, *356*, 80−87.

(15) Låte, L.; Rundereim, J. I.; Blekkan, E. A. Selective Combustion of Hydrogen in the Presence of Hydrocarbons: 1. Pt-Based Catalysts. *Appl. Catal. A Gen.* **2004**, *262*, 53−61.

(16) Ren, X.; Lv, Q.; Liu, L.; Liu, B.; Wang, Y.; Liu, A.; Wu, G. Current Progress of Pt and Pt-Based Electrocatalysts Used for Fuel Cells. *Sustain. Energy Fuels* **2020**, *4*, 15−30.

(17) Maestri, M.; Vlachos, D. G.; Beretta, A.; Forzatti, P.; Groppi, G.; Tronconi, E. Dominant Reaction Pathways in the Catalytic Partial Oxidation of CH_4 on Rh. *Top. Catal.* **2009**, *52*, 1983−1988.

(18) Chin, Y.-H.; Buda, C.; Neurock, M.; Iglesia, E. Selectivity of Chemisorbed Oxygen in C-H Bond Activation and CO Oxidation and Kinetic Consequences for CH_4-O_2 Catalysis on Pt and Rh Clusters. *J. Catal.* **2011**, *283*, 10−24.

(19) Linstrom, P.; Mallard, W. NIST Standard Reference Database Number 69; *NIST Chemistry WebBook*; http://webbook.nist.gov (accessed 2020-06-01).

(20) Hellsing, B.; Kasemo, B.; Zhdanov, V. P. Kinetics of the Hydrogen-Oxygen Reaction on Platinum. *J. Catal.* **1991**, *132*, 210−228.

(21) Wahnström, T.; Fridell, E.; Ljungström, S.; Hellsing, B.; Kasemo, B.; Rosén, A. Determination of the Activation Energy for OH Desorption in the H_2 + O_2 Reaction on Polycrystalline Platinum. *Surf. Sci. Lett.* **1989**, *223*, L905−L912.

(22) Gorodetskii, V. V. Experimental Evidence of Propagating Waves in Hydrogen Oxidation on Platinum-Group Metals (Pt, Rh, Ir). *Kinet. Catal.* **2009**, *50*, 304−313.

(23) Norton, P. R. A Photoelectron Spectroscopic Study of the Adsorption and Reactivity of Oxygen on Platinum. *J. Catal.* **1975**, *36*, 211−223.

(24) Chin, Y. H.; Buda, C.; Neurock, M.; Iglesia, E. Reactivity of Chemisorbed Oxygen Atoms and Their Catalytic Consequences during CH_4-O_2 Catalysis on Supported Pt Clusters. *J. Am. Chem. Soc.* **2011**, *133*, 15958−15978.

(25) García-Diéguez, M.; Chin, Y. H. C.; Iglesia, E. Catalytic Reactions of Dioxygen with Ethane and Methane on Platinum Clusters: Mechanistic Connections, Site Requirements, and Consequences of Chemisorbed Oxygen. *J. Catal.* **2012**, *285*, 260−272.

(26) García-Diéguez, M.; Hibbitts, D. D.; Iglesia, E. Hydrogen Chemisorption Isotherms on Platinum Particles at Catalytic Temperatures: Langmuir and Two-Dimensional Gas Models Revisited. *J. Phys. Chem. C* **2019**, *123*, 8447−8462.

(27) Miller, J. T.; Schreier, M.; Kropf, A. J.; Regalbuto, J. R. A Fundamental Study of Platinum Tetraammine Impregnation of Silica: 2. The Effect of Method of Preparation, Loading, and Calcination Temperature on (Reduced) Particle Size. *J. Catal.* **2004**, *225*, 203−212.

(28) Thomas, J. M. *Handbook of Heterogeneous Catalysis*, 2nd ed.; Ertl, G., Knözinger, H., Schüth, F., Weitkamp, J., Eds.; Wiley-VCH: Weinheim, Germany, 2008; Vols. *1*−*8*.

(29) Almithn, A. S.; Hibbitts, D. D. Supra-Monolayer Coverages on Small Metal Clusters and Their Effects on H_2 Chemisorption Particle Size Estimates. *AIChE J.* **2018**, *64*, 3109−3120.

(30) Schroeder, V.; Holtappels, K. Explosion Characteristics of Hydrogen-Air and Hydrogen-Oxygen Mixtures at Elevated Pressures. *International Conference on Hydrogen Safety*, 2005.

(31) Kresse, G.; Hafner, J. Ab Initio Molecular-Dynamics Simulation of Liquid-Metal-Amorphous-Semiconductor Transition in Germanium. *Phys. Rev. B* **1994**, *49*, 14251−14269.

(32) Kresse, G.; Furthmüller, J. Efficient Iterative Schemes for *Ab Initio* Total-Energy Calculations Using a Plane-Wave Basis Set. *Phys. Rev. B* **1996**, *54*, 11169−11186.

(33) Kresse, G.; Furthmüller, J. Efficiency of Ab-Initio Total Energy Calculations for Metals and Semiconductors Using a Plane-Wave Basis Set. *Comput. Mater. Sci.* **1996**, *6*, 15−50.

(34) Blöchl, P. E. Projector Augmented-Wave Method. *Phys. Rev. B* **1994**, *50*, 17953−17979.

(35) Kresse, G.; Joubert, D. From Ultrasoft Pseudopotentials to the Projector Augmented-Wave Method. *Phys. Rev. B - Condens. Matter Mater. Phys.* **1999**, *59*, 1758−1775.
(36) Monkhorst, H. J.; Pack, J. D. Special Points for Brillouin-Zone Integrations. *Phys. Rev. B* **1976**, *13*, 5188−5192.
(37) Perdew, J. P.; Chevary, J. A.; Vosko, S. H.; Jackson, K. A.; Pederson, M. R.; Singh, D. J.; Fiolhais, C. Atoms, Molecules, Solids, and Surfaces: Applications of the Generalized Gradient Approximation for Exchange and Correlation. *Phys. Rev. B* **1992**, *46*, 6671−6687.
(38) Van Hardeveld, R.; Hartog, F. The Statistics of Surface Atoms and Surface Sites on Metal Crystals. *Surf. Sci.* **1969**, *15*, 189−230.
(39) Arblaster, J. W. Crystallographic Properties of Platinum. *Platin. Met. Rev.* **2006**, *50*, 118−119.
(40) Henkelman, G.; Jónsson, H. Improved Tangent Estimate in the Nudged Elastic Band Method for Finding Minimum Energy Paths and Saddle Points. *J. Chem. Phys.* **2000**, *113*, 9978−9985.
(41) Jónsson, H.; Mills, G.; Jacobsen, K. W. Nudged Elastic Band Method for Finding Minimum Energy Paths of Transitions. *Classical and Quantum Dynamics in Condensed Phase Simulations* **1998**, 385−404.
(42) Henkelman, G.; Jónsson, H. A Dimer Method for Finding Saddle Points on High Dimensional Potential Surfaces Using Only First Derivatives. *J. Chem. Phys.* **1999**, *111*, 7010−7022.
(43) Henkelman, G.; Jónsson, H. A Dimer Method for Finding Saddle Points on High Dimensional Potential Surfaces Using Only First Derivatives. *J. Chem. Phys.* **1999**, *111*, 7010−7022.
(44) Kravchenko, P.; Krishnan, V.; Hibbitts, D. Mechanism and Effects of Coverage and Particle Morphology on Rh-Catalyzed NO-H_2 Reactions. *J. Phys. Chem. C* **2020**, *124*, 13291−13303.
(45) Mei, D.; Lercher, J. A. Mechanistic Insights into Aqueous Phase Propanol Dehydration in H-ZSM-5 Zeolite. *AIChE J.* **2017**, *63*, 172−184.
(46) Zhi, Y.; Shi, H.; Mu, L.; Liu, Y.; Mei, D.; Camaioni, D. M.; Lercher, J. A. Dehydration Pathways of 1-Propanol on HZSM-5 in the Presence and Absence of Water. *J. Am. Chem. Soc.* **2015**, *137*, 15781−15794.
(47) Maymo, J. A.; Smith, J. M. Catalytic Oxidation of Hydrogen—Intrapellet Heat and Mass Transfer. *AIChE J.* **1966**, *12*, 845−854.
(48) Leder, F.; Butt, J. B. Surface Catalysis of the Hydrogen-oxygen Reaction on Platinum at Low Temperatures. *AIChE J.* **1966**, *12*, 718−721.
(49) Hibbitts, D. D.; Loveless, B. T.; Neurock, M.; Iglesia, E. Mechanistic Role of Water on the Rate and Selectivity of Fischer−Tropsch Synthesis on Ruthenium Catalysts. *Angew. Chemie - Int. Ed.* **2013**, *52*, 12273−12278.
(50) Zhao, Y. F.; Yang, Y.; Mims, C.; Peden, C. H. F.; Li, J.; Mei, D. Insight into Methanol Synthesis from CO_2 Hydrogenation on Cu(1 1 1): Complex Reaction Network and the Effects of H_2O. *J. Catal.* **2011**, *281*, 199−211.
(51) Desai, S.; Neurock, M. A First Principles Analysis of CO Oxidation over Pt and Pt66.7%Ru33.3% (111) Surfaces. *Electrochim. Acta* **2003**, *48*, 3759−3773.
(52) Ricciardulli, T.; Adams, J. S.; DeRidder, M.; van Bavel, A. P.; Karim, A. M.; Flaherty, D. W. H_2O-Assisted O_2 Reduction by H_2 on Pt and PtAu Bimetallic Nanoparticles: Influences of Composition and Reactant Coverages on Kinetic Regimes, Rates, and Selectivities. *J. Catal.* **2021**, *404*, 661−678.
(53) Borg, Øy.; Storsæter, S.; Eri, S.; Wigum, H.; Rytter, E.; Holmen, A. The Effect of Water on the Activity and Selectivity for γ-Alumina Supported Cobalt Fischer−Tropsch Catalysts with Different Pore Sizes. *Catal. Lett.* **2006**, *107*, 95−102.
(54) Krishnamoorthy, S.; Tu, M.; Ojeda, M. P.; Pinna, D.; Iglesia, E. An Investigation of the Effects of Water on Rate and Selectivity for the Fischer−Tropsch Synthesis on Cobalt-Based Catalysts. *J. Catal.* **2002**, *211*, 422−433.
(55) Hilmen, A. M.; Schanke, D.; Hanssen, K. F.; Holmen, A. Study of the Effect of Water on Alumina Supported Cobalt Fischer−Tropsch Catalysts. *Appl. Catal. A Gen.* **1999**, *186*, 169−188.
(56) Koverga, A. A.; Flórez, E.; Jimenez-Orozco, C.; Rodriguez, J. A. Spot the Difference: Hydrogen Adsorption and Dissociation on Unsupported Platinum and Platinum-Coated Transition Metal Carbides. *Phys. Chem. Chem. Phys.* **2021**, *23*, 20255−20267.
(57) Mukherjee, J.; Linic, S. First-Principles Investigations of Electrochemical Oxidation of Hydrogen at Solid Oxide Fuel Cell Operating Conditions. *J. Electrochem. Soc.* **2007**, *154*, B919.
(58) Whittaker, T.; Kumar, K. B. S.; Peterson, C.; Pollock, M. N.; Grabow, L. C.; Chandler, B. D. H_2 Oxidation over Supported Au Nanoparticle Catalysts: Evidence for Heterolytic H_2 Activation at the Metal-Support Interface. *J. Am. Chem. Soc.* **2018**, *140*, 16469−16487.
(59) Mansour, H.; Iglesia, E. Mechanistic Connections between CO_2 and CO Hydrogenation on Dispersed Ruthenium Nanoparticles. *J. Am. Chem. Soc.* **2021**, *143*, 11582−11594.
(60) Ojeda, M.; Nabar, R.; Nilekar, A. U.; Ishikawa, A.; Mavrikakis, M.; Iglesia, E. CO Activation Pathways and the Mechanism of Fischer−Tropsch Synthesis. *J. Catal.* **2010**, *272*, 287−297.
(61) Loveless, B. *C-O Bond Activation and C-C Bond Formation Paths in Catalytic CO Hydrogenation*. Ph.D. Dissertation, University of California, Berkeley, CA, 2012.
(62) Yik, E.; Hibbitts, D.; Wang, H.; Iglesia, E. Hydrogenation and C-S Bond Activation Pathways in Thiophene and Tetrahydrothiophene Reactions on Sulfur-Passivated Surfaces of Ru, Pt, and Re Nanoparticles. *Appl. Catal. B Environ.* **2021**, *291*, 119797.
(63) Jinnouchi, R.; Kodama, K.; Morimoto, Y. DFT Calculations on H, OH and O Adsorbate Formations on Pt(111) and Pt(332) Electrodes. *J. Electroanal. Chem.* **2014**, *716*, 31−44.
(64) Seriani, N.; Pompe, W.; Ciacchi, L. C. Catalytic Oxidation Activity of Pt_3O_4 Surfaces and Thin Films. *J. Phys. Chem. B* **2006**, *110*, 14860−14869.
(65) Chou, T. Y.; Hwang, C. P.; Yeh, C. T. Graphic Determination of Kinetic Parameters in Temperature-Programmed Desorption of Oxygen from Alumina-Supported PdO. *J. Therm. Anal.* **1996**, *46*, 305−315.
(66) Chin, Y. H. C.; García-Diéguez, M.; Iglesia, E. Dynamics and Thermodynamics of Pd-PdO Phase Transitions: Effects of Pd Cluster Size and Kinetic Implications for Catalytic Methane Combustion. *J. Phys. Chem. C* **2016**, *120*, 1446−1460.
(67) Serra-Maia, R.; Bellier, M.; Chastka, S.; Tranhuu, K.; Subowo, A.; Rimstidt, J. D.; Usov, P. M.; Morris, A. J.; Michel, F. M. Mechanism and Kinetics of Hydrogen Peroxide Decomposition on Platinum Nanocatalysts. *ACS Appl. Mater. Interfaces* **2018**, *10*, 21224−21234.
(68) Flaherty, D. W. Direct Synthesis of H_2O_2 from H_2 and O_2 on Pd Catalysts: Current Understanding, Outstanding Questions, and Research Needs. *ACS Catal.* **2018**, *8*, 1520−1527.
(69) Dissanayake, D. P.; Lunsford, J. H. The Direct Formation of H_2O_2 from H_2 and O_2 over Colloidal Palladium. *J. Catal.* **2003**, *214*, 113−120.
(70) Lewis, R. J.; Ntainjua, E. N.; Morgan, D. J.; Davies, T. E.; Carley, A. F.; Freakley, S. J.; Hutchings, G. J. Improving the Performance of Pd Based Catalysts for the Direct Synthesis of Hydrogen Peroxide via Acid Incorporation during Catalyst Synthesis. *Catal. Commun.* **2021**, *161*, 106358.
(71) Burch, R.; Ellis, P. R. An Investigation of Alternative Catalytic Approaches for the Direct Synthesis of Hydrogen Peroxide from Hydrogen and Oxygen. *Appl. Catal. B Environ.* **2003**, *42*, 203−211.
(72) Lewis, R. J.; Hutchings, G. J. Recent Advances in the Direct Synthesis of H_2O_2. *ChemCatChem.* **2019**, *11*, 298−308.
(73) Barnes, A.; Lewis, R. J.; Morgan, D. J.; Davies, T. E.; Hutchings, G. J. Improving Catalytic Activity towards the Direct Synthesis of H_2O_2 through Cu Incorporation into AuPd Catalysts. *Catalysts* **2022**, *12*, 1396.
(74) Satterfield, C. N.; Stein, T. W. Homogeneous Decomposition of Hydrogen Peroxide Vapor. *J. Phys. Chem.* **1957**, *61*, 537−540.
(75) Satterfield, C. N.; Reid, R. C.; Wechsler, A. E. Chemical Kinetics in Porous Walled Reactors: The Decomposition of Hydrogen Peroxide Vapor. *AIChE J.* **1963**, *9*, 168−175.

https://doi.org/10.1021/acs.jpcc.2c08826
J. Phys. Chem. C 2023, 127, 4553−4569

(76) Satterfield, C.; Stein, T. Decomposition of Hydrogen Peroxide Vapor on Relatively Inert Surfaces. *Ind. Eng. Chem.* **1957**, *49*, 1173−1180.
(77) Campbell, C. T.; Sellers, J. R. V. The Entropies of Adsorbed Molecules. *J. Am. Chem. Soc.* **2012**, *134*, 18109−18115.
(78) Leung, S. L.; Hibbitts, D.; Gárcia-Diéguez, M.; Iglesia, E. Binding and Exchange Reactions of Hydrogen Isotopes on Surfaces of Dispersed Pt Nanoparticles. *J. Phys. Chem. C* **2022**, *126*, 3923−3938.
(79) Evans, M. G.; Polanyi, M. Further Considerations on the Thermodynamics of Chemical Equilibria and Reaction Rates. *Trans. Faraday Soc.* **1936**, *32*, 1333−1360.
(80) Allian, A. D.; Takanabe, K.; Fujdala, K. L.; Hao, X.; Truex, T. J.; Cai, J.; Buda, C.; Neurock, M.; Iglesia, E. Chemisorption of CO and Mechanism of CO Oxidation on Supported Platinum Nanoclusters. *J. Am. Chem. Soc.* **2011**, *133*, 4498−4517.
(81) Carballo, J. M. G.; Yang, J.; Holmen, A.; García-Rodríguez, S.; Rojas, S.; Ojeda, M.; Fierro, J. L. G. Catalytic Effects of Ruthenium Particle Size on the Fischer−Tropsch Synthesis. *J. Catal.* **2011**, *284*, 102−108.
(82) Yang, J.; Tveten, E. Z.; Chen, D.; Holmen, A. Understanding the Effect of Cobalt Particle Size on Fischer−Tropsch Synthesis: Surface Species and Mechanistic Studies by SSITKA and Kinetic Isotope Effect. *Langmuir* **2010**, *26*, 16558−16567.

https://doi.org/10.1021/acs.jpcc.2c08826
J. Phys. Chem. C 2023, 127, 4553−4569